A multi-satellite framework to rapidly evaluate extreme biosphere cascades: the Western US 2021 drought and heatwave

Andrew F. Feldman[1,2], Zhen Zhang[3], Yasuko Yoshida[4], Pierre Gentine[5], Abhishek Chatterjee[6], Dara Entekhabi[7], Joanna Joiner[8], Benjamin Poulter[1]

[1]Biospheric Sciences Laboratory, NASA Goddard Space Flight Center, Greenbelt, MD, USA
[2]NASA Postdoctoral Program, NASA Goddard Space Flight Center, Greenbelt, MD, USA
[3]Earth System Science Interdisciplinary Center, University of Maryland, College Park, MD, USA
[4]Science Systems and Applications, Inc. (SSAI), Lanham, MD, USA
[5]Department of Earth and Environmental Engineering, Columbia University, New York, New York, USA
[6]Jet Propulsion Laboratory, California Institute of Technology, Pasadena, CA, USA
[7]Department of Civil and Environmental Engineering, Massachusetts Institute of Technology, 15 Vassar St., Cambridge, Massachusetts, 02139, USA
[8]Atmospheric Chemistry and Dynamics Laboratory, NASA Goddard Space Flight Center, Greenbelt, MD, USA

Abstract

The increasing frequency and intensity of climate extremes and complex ecosystem responses motivate the need for integrated observational studies at low-latency to determine biosphere responses and carbon-climate feedbacks. Here, we develop a satellite-based rapid attribution workflow and demonstrate its use at a 1–2-month latency to attribute drivers of the carbon cycle feedbacks during the 2020-2021 Western US drought and heatwave. In the first half of 2021, concurrent negative photosynthesis anomalies and large positive column CO_2 anomalies were detected with satellites. Using a simple atmospheric mass balance approach, we estimate a surface carbon efflux anomaly of 132 TgC in June 2021, a magnitude corroborated independently with a dynamic global vegetation model. Integrated satellite observations of hydrologic processes, representing the soil-plant-atmosphere continuum (SPAC), show that these surface carbon flux anomalies are largely due to substantial reductions in photosynthesis because of a spatially widespread moisture-deficit propagation through the SPAC between 2020 and 2021. A causal model indicates deep soil moisture stores partially drove photosynthesis, maintaining its values in 2020 and driving its declines throughout 2021. The causal model also suggests legacy effects may have amplified photosynthesis deficits in 2021 beyond the direct effects of environmental forcing. The integrated, observation framework presented here provides a valuable first assessment of a biosphere extreme response and an independent testbed for improving drought propagation and mechanisms in models. The rapid identification of extreme carbon anomalies and hotspots can also aid mitigation and adaptation decisions.

1. Introduction

There is a growing need for timely information on terrestrial carbon flux response to climate extremes to better understand their drivers through attribution studies and to inform climate mitigation and adaptation policies (Ciais et al., 2014; Frank et al., 2015; Schimel et al., 2015; Sellers et al., 2018). Low-latency studies, within 2-3 months of an event, can enable rapid attribution and facilitate monitoring and management either during or directly following extreme

events (Reichstein et al., 2013; Zscheischler et al., 2013). The terrestrial biosphere removes the equivalent of about 25% of global annual anthropogenic emissions (Friedlingstein et al., 2021) and drives inter-annual variability in atmospheric CO_2 concentrations (Wang et al., 2013). While increasing anthropogenic CO_2 concentrations have been shown to increase biosphere carbon uptake with CO_2 fertilization of vegetation (Ainsworth and Long, 2005; Keenan et al., 2014), increasing drought frequency and intensity (Sheffield and Wood, 2008) may offset this response substantially (Reichstein et al., 2013; Jakob Zscheischler et al., 2014). These extreme events may leave long-lasting negative imprints on the biosphere (Ciais et al., 2005; Green et al., 2019) because slow biospheric carbon uptake can be compensated by rapid carbon releases due to extremes and disturbances (Körner, 2003). These extremes can also cause crossing of landscape thresholds and activation of biosphere mechanisms not typically experienced at that location (Grünzweig et al., 2022). Furthermore, droughts and heatwaves can amplify carbon uptake interannual variability (Ahlström et al., 2015; Luo and Keenan, 2022; Poulter et al., 2014), confounding how fossil CO_2 mitigation will be detected in the atmosphere at interannual timescales. As such, monitoring and improving the short-term attribution of extreme biosphere responses is becoming increasingly important for the global carbon cycle community.

Traditional remote sensing vegetation indices from the Moderate Resolution Imaging Spectroradiometer (MODIS) and others provide a means to rapidly identify vegetation anomalies as a proxy for extreme photosynthetic fluxes (Zscheischler et al., 2013). Additionally, satellite observations of column-integrated dry mole fraction of CO_2 (XCO_2) could provide a complementary capability to detect total biosphere carbon flux anomalies, which also integrate respiration and wildfire emissions in natural ecosystems (Crisp et al., 2004). Satellite XCO_2 retrievals are limited by instrument noise and confounding background atmospheric transport (Buchwitz et al., 2021, 2017; Hakkarainen et al., 2016), and are mainly used to constrain the global terrestrial carbon cycle interannual variability (Patra et al., 2017). Nevertheless, satellite XCO_2 observations are available at the low latency (~1-2 months) and global scale needed to monitor biosphere response to large scale climate extremes (Peters et al., 2007; Schimel et al., 2015). Amongst debate in how sensitive XCO_2 anomalies are to surface fluxes (Chevallier, 2018; Schuh et al., 2022), there is evidence that spatially concentrated, extreme surface CO_2 fluxes imprint on sub-yearly variability of NASA's Orbiting Carbon Observatory-2 (OCO-2) XCO_2 retrievals (Chatterjee et al., 2017; Feldman et al., 2023; Liu et al., 2017; Weir et al., 2021).

To identify drivers of biosphere extremes, the existing constellation of Earth-observing satellites can monitor the soil-plant-atmosphere-continuum (SPAC) including surface soil moisture (Soil Moisture Active Passive; SMAP), terrestrial water storage (TWS from Gravity Recovery and Climate Experiment; GRACE), vegetation water content (vegetation optical depth (VOD) from SMAP), gross primary productivity (GPP from MODIS), boundary layer vapor pressure deficit (Atmospheric Infrared Sounder; AIRS), and precipitation (Global Precipitation Measurement; GPM). Since these data are available globally within 1–2-month latency, these observations alone can rapidly attribute major drivers of biospheric anomalies, supporting ground network and modeling efforts. Recent studies have revealed that the drought impacts on the biosphere are complex, including compounded and lagged biosphere legacy effects (Anderegg et al., 2020; Bastos et al., 2020). Given that these biosphere responses to extremes are not well characterized in Earth system models (ESMs) and dynamic global vegetation models (DGVMs) (Bastos et al., 2021; De Kauwe et al., 2015; Egea et al., 2011; Powell et al., 2013), satellite observations can be used as a benchmark for these biosphere models in attributing biosphere responses to droughts and heatwaves (Anderegg et al., 2015; Byrne et al., 2021).

Here, our objective is to demonstrate a satellite-based workflow that can detect extreme biospheric flux anomalies and identify their climatic drivers at low latency. Apart from its low latency, the workflow's observation use provides fundamental insights into terrestrial biosphere behavior under extreme climate conditions and benchmarks for modeled behavior. Furthermore, the workflow's use of a breadth of observations at sub-seasonal timescales allows pinpointing specific and/or combinations of soil-plant-atmosphere variables responsible for carbon flux anomalies, given complex behavior during extremes that obscures attribution.

We specifically apply this framework to address: how did the Western US biosphere respond to the 2020-2021 extreme climate event? This event was characterized by unprecedented agricultural and municipal water shortages (Fountain, 2021; Williams et al., 2022) as well as a 1000-year heatwave in the Pacific Northwest in spring 2021 (Philip et al., 2021). The Western US is becoming a hotspot for megadroughts and increasing drought frequency (Cook et al., 2021) and its biosphere dynamics are strongly linked to water availability (Short Gianotti et al., 2019). This combination will result in the Western US increasingly contributing to the global carbon cycle interannual variability, similarly to Australia (Haverd et al., 2017). To demonstrate the low-latency feature of the workflow, the analysis took place with data available by September 2021.

2. Materials and Methods

2.1 Extreme Biosphere Cascade Detection and Analysis Workflow

We organize our observational analysis into a low-latency framework for evaluating effects of extreme climate anomalies on the terrestrial biosphere that is transferable to future events. The workflow is purposely flexible and guides the main analyses that should be conducted in a rapid attribution study to inform other analyses of the same event, to provide ample information for future meta-analyses, and to aid in biosphere model development and testing. All methods were independently developed and validated to varying degrees previously but are organized here into four steps.

The first two steps include identifying the spatiotemporal domain of climatic and CO_2 flux anomalies (Fig. 1; Panels I and II). The purpose of these steps is to initially define the spatiotemporal domain of the carbon-climate feedback and initially identify the interacting carbon and climate variables. The spatiotemporal domain should be defined using a standardized anomaly metric (i.e. z-score, percentiles) (Slette et al., 2019), though we acknowledge a range of available anomaly detection methods and subjectivity given challenges in defining spatiotemporal bounds of extreme events (Flach et al., 2017; Meroni et al., 2019; Nicolai-Shaw et al., 2017; Vicca et al., 2016; Zscheischler et al., 2014).

Step I's purpose is to determine where and when a carbon flux anomaly occurs and which carbon components may be responsible (Fig. 1 Panel I). Such large anomalies can be searched for based on knowledge of an ongoing climatic event (i.e., known ongoing drought in a region) or based on a global search for anomalies with low-latency datasets (Zscheischler et al., 2013). "Extreme" has different definitions across the literature. We recommend detecting anomalies at the tails of the variable's distribution outside of typical variability based on user-defined z-score or percentile thresholds (Smith, 2011; Yang et al., 2023; Zscheischler et al., 2013). Note that the carbon anomaly's magnitude, duration, and/or spatial extent can be the extreme feature to be investigated (Reichstein et al., 2013; Yang et al., 2023). In our framework, Step I first includes detecting the total carbon anomaly (i.e., with XCO_2), indicating a large total CO_2 flux anomaly, and then detection of individual CO_2 flux components. However, given that some CO_2 flux

anomalies may not be observed with XCO_2 from greenhouse gas satellites (Feldman et al., 2023), individual CO_2 component anomaly detection (i.e., vegetation indices) should be initiated, especially if there is a known climate anomaly. Furthermore, we demonstrate a rough estimation of surface carbon fluxes that can be used in this step, acknowledging its uncertainty and its usefulness only under specific spatiotemporal conditions (Feldman et al., 2023).

Step II involves determining the driving climate anomaly variables (Fig. 1 Panel II). It should also expand on the spatiotemporal domain determined in Step I. For temporal considerations, with an expected time lag in the biosphere response, this step should determine the event beginning when the climate anomaly initiates a cascade before the identified carbon anomaly. For spatial considerations, climate anomalies may extend beyond the spatial domain of the Step I identified carbon response since different biomes respond to extreme climate to varying degrees (Smith, 2011). Some subjectivity is expected when defining the spatiotemporal bounds of the study. Note that Step II can be completed before Step I if the interest is in determining whether a climate anomaly resulted in a carbon anomaly.

Following the spatiotemporal domain definition, Step III is a cascade analysis evaluating how climate anomalies temporally propagate from atmosphere to soil to the surface carbon flux component (Fig. 1; Panel III). The purpose is to attribute carbon anomaly drivers by establishing links between climate and carbon variables and identifying timing and magnitude attributes of the anomalies. Climatic extremes, especially droughts, typically exhibit a hydrologically-linked cascade, or an anomaly propagation from atmosphere to land surface variables with a time lag and changing amplitude in each variable it effects (Farahmand et al., 2021). We extend the cascade definition here to study how the hydrologic cascade propagates into the biosphere and focus on the utility of evaluating the time lags. The choice of variables to evaluate in the cascade analysis should be informed by Steps I and II, but it is suggested that at least precipitation, soil moisture, and VPD are consulted to evaluate observation-based propagation of a warm and/or dry anomaly into the biosphere. The use of more variables may become limited by computational needs (Ciais et al., 2014), though the datasets presented here are all available on public, user-friendly databases. The spatial extent, duration, and magnitude of all anomalies should be computed in this step for ease of comparison to other events and application in meta-analyses (Reichstein et al., 2013; Slette et al., 2019).

The fourth step is a targeted time series analysis to statistically test detailed links between dry/hot anomalies and a biosphere response within the cascade. Results from the statistical analyses of observed ecosystem response to extreme climate can also be used to test aspects of DGVM outputs. Regression models can be consulted, such as those that detect causality via Granger Causality using observations (Feldman et al., 2020; Green et al., 2017). While links between these variables can be known from previous analyses, it is suggested that a causal model is used to evaluate the anomaly during the event due to potential changes in ecosystem function during extremes (Bastos et al., 2020).

Each analysis step progressively allows more detailed analysis of biosphere response drivers. Additionally, given that each analysis partially relies on results from the previous step, each step increases in need for adaptation to the specific location and event. As such, it is expected that the cascade analysis and time series analysis will require more adaptation for use on different events and locations.

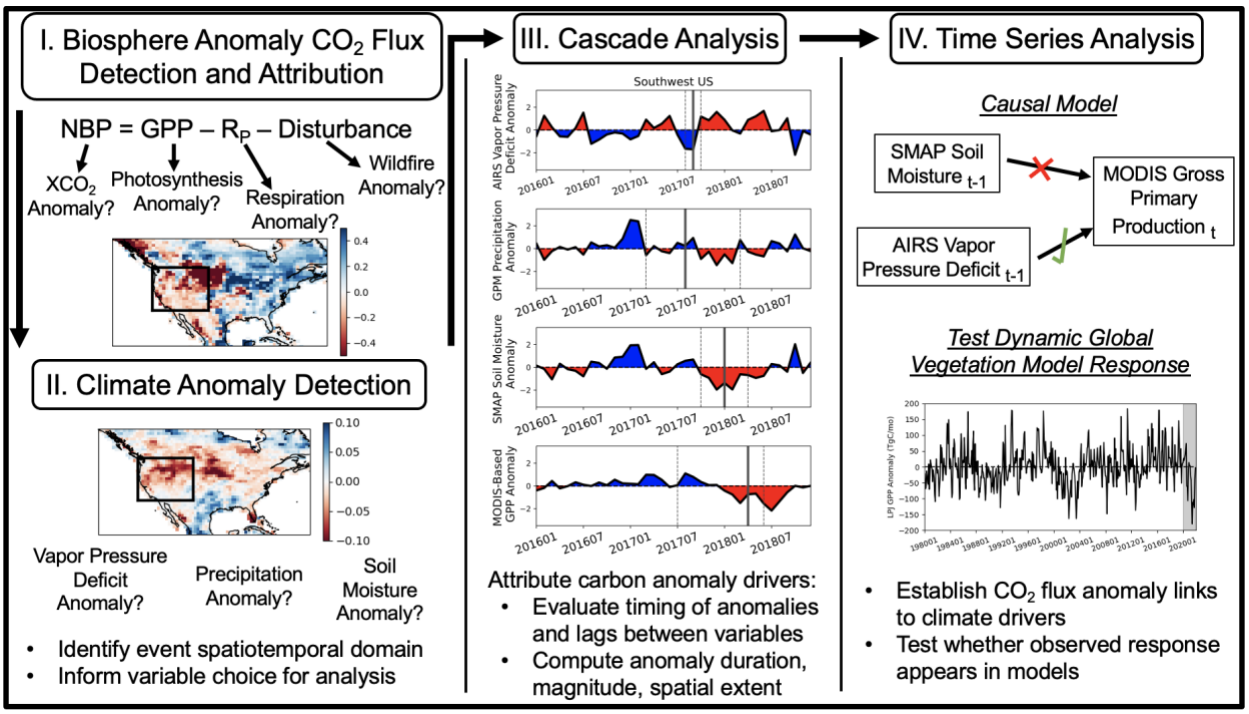

Fig. 1. Low-latency, remote sensing-based framework to evaluate extreme carbon-climate feedbacks and attribute drivers. (I) Detection and attribution of CO_2 flux anomaly during the extreme event. (II) Spatiotemporal detection of climatic anomaly. (III) Cascade analysis of environmental drivers of the CO_2 flux anomaly. (IV) Time series analysis to determine linkages between environmental drivers and CO_2 flux during the event.

2.2 Study Domain

Based on our analysis in Steps I and II, we identified the study region as the Western US (latitude: 33°N-49°N, longitude: 125°W-104°W), which is characterized by predominantly semi-arid ecosystems and localized temperate forest ecosystems. These steps also identified the main study period as January 2020 to July 2021. We applied the framework to the extreme drought and heatwave of spring 2021 that is superimposed on a year of large water deficits and high temperatures beginning in 2020 (Dannenberg et al., 2022; Williams et al., 2022). Note that this study took place using data available in September 2021.

2.3 Datasets

Our workflow uses satellite-based carbon cycle variables responding to climate anomalies including OCO-2 XCO_2 and solar induced fluorescence (SIF) between 2014-2021 at 16-day and 3kmx3km resolution (OCO-2-Science-Team et al., 2020a, 2020b), and MODIS-based FluxSat GPP between 2003-2021 at daily and 1°x1.25° resolution (Joiner and Yoshida, 2021, 2020). GPP is mainly used to represent vegetation response while SIF is only used as an independent photosynthesis proxy in Step IV. Quick Fire Emissions Dataset (QFED) biomass burning emissions at daily and 0.1°x0.1° resolution (Koster et al., 2015) and CarbonMonitor fossil fuel emissions reported in the Western US states in our region (Liu et al., 2020) were used as auxiliary datasets to assess other contributions to surface carbon fluxes (Fig. S1).

The workflow also attempts to represent diverse components of the soil-plant-atmosphere continuum to attribute complex drivers of extreme carbon anomalies. These satellite observations

include atmospheric variables from AIRS boundary layer air temperature, specific humidity, and vapor pressure deficit (VPD) between 2003-2021 at daily and 1°x1° resolution (Teixeira, 2013) and from GPM rainfall between 2010-2021 at daily and 0.1°x0.1° resolution (Huffman et al., 2019). We also used land surface variables including deeper water stores from GRACE TWS between 2002-2021 at monthly and 0.5°x0.5° resolution (Wiese et al., 2019) as well as surface soil moisture and vegetation water content (VOD) from SMAP between 2015-2021 at 1-3 day and 9kmx9km grid scales using an alternative algorithm that is independent of MODIS measurements (Feldman et al., 2021).

Several other datasets were used as ancillary support. CarbonTracker reanalysis (CT2019B) assimilated XCO_2 profiles and total surface carbon fluxes at 3-hourly and 1°x1° resolution were used to test OCO-2 XCO_2-based flux estimate methods (Peters et al., 2007). Global Precipitation Climatology Project (GPCP) rainfall between 1979-2021 at monthly and 2.5°x2.5° resolution were used to report a drought index, or standard precipitation index (SPI) (Mckee et al., 1993; Slette et al., 2020). Though at longer latency, GPCP monthly rainfall data were used in the causal regression analysis given its greater sampling period (Adler et al., 2003). We additionally used estimated maximum rooting depths at a 0.5° resolution (Fan et al., 2017).

Datasets were linearly resampled to monthly and to 1°x1° grid scales. FluxSat GPP and GPCP were retained on their 1°x1.25° and 2.5°x2.5° grid scales, respectively. Standardized z-score anomalies were computed for each variable by subtracting seasonal long-term climatology and dividing by their standard deviation. Z-score anomalies are a standard metric to detect larger anomalies at the tails of the variable's distribution, especially those more than a standard deviation from the mean, though more sophisticated non-parametric methods can be alternatively used (Meroni et al., 2019). For consistency between datasets, anomalies were computed based on climatological monthly means between January 2015 and December 2020. We removed long-term and seasonal amplitude trends in XCO_2 by detrending each individual month separately.

2.4. Step I: CO_2 Flux Anomaly Detection and Component Analysis

We evaluated OCO-2 XCO_2 anomalies first to detect CO_2 flux anomalies during 2020-2021, when known hot and dry anomalies were occurring in the Western US. We then evaluated CO_2 flux components that would contribute to the total CO_2 flux anomaly, including MODIS-based GPP and QFED biomass burning anomalies.

2.5 Step II: Climate Anomaly Detection

We initially evaluated SMAP soil moisture and AIRS vapor pressure deficit anomalies before the detected carbon anomalies to augment the spatiotemporal definition as well as to initially attribute the carbon component anomalies to specific climatic anomalies.

2.6 XCO_2 Profile Analysis and Estimation

We evaluated the ability for XCO_2 anomalies to detect surface biosphere anomalies in the Western US, which would ultimately augment Step I. These XCO_2 anomalies were correlated against biosphere-only fluxes (i.e., excluding anthropogenic and land-use land cover changes emissions): namely monthly fluxes modeled by LPJ NBP and MODIS-based FluxSat GPP estimates. Given strong influences of atmospheric transport on XCO_2, we identified background regions that contribute air that mixes with XCO_2 within the Western US region. MERRA2 wind vectors reveal the Pacific Ocean as the consistent upwind region of the Western US (Feldman et al., 2023). Therefore, concurrent analysis of background Pacific Ocean XCO_2 conditions offer

insights into whether spatially integrated XCO_2 anomalies within the Western US have contributions from a surface instead of upwind source.

We additionally used an established mass balance model to translate the XCO_2 anomaly to a rough estimation of the surface CO_2 flux anomaly. Specifically, XCO_2 anomaly enhancements (difference between Western US and background Pacific Ocean XCO_2 anomalies) were used to estimate the total surface carbon anomalies in the Western US using:

$$Q = (\Delta XCO_2)(V)(L)\left(M_{exp}\right)(M)(C) \qquad (1)$$

where the carbon efflux anomaly from the surface (Q) depends on the enhancement of the target area's XCO_2 anomaly above the upwind region's XCO_2 anomaly (ΔXCO_2; $ppmCO_2$ units), the wind velocity (V; km/mo units), and effective length of the surface emission region (L; km units) (Buchwitz et al., 2017; Liu et al., 2021; Pandey et al., 2021). The other terms (i.e., M_{exp}, M, C; units of $TgC/km^2/ppmCO_2$, unitless, and unitless, respectively) are conversion factors and atmospheric transport assumptions (see SI). A bootstrapping approach was used to estimate the 90% confidence intervals of Q.

This approach was evaluated in detail in a recent study and we note that it is only feasible under select conditions, especially under simpler advection conditions as in the Western US and for extreme fluxes (Feldman et al., 2023). We emphasize that XCO_2 anomalies serve as a complementary, independent form of detecting carbon-climate feedbacks and thus inability of XCO_2 anomalies to detect and/or estimate an extreme flux does not hinder the procedure here.

2.7 Reference DGVM Run

The Lund-Potsdam-Jena Wald Schnee and Landshaft (LPJ-wsl) Biosphere Model was used here as an independent model-based source of information about surface CO_2 flux anomalies, acknowledging uncertainty in individual GPP and respiration response to extremes (Sitch et al., 2003). We evaluated LPJ for its estimates of cumulative net biome productivity (NBP) and contribution from GPP. LPJ serves as an independent DGVM to compare outputs with, which is informative given its carbon flux performance typically near the average of multi-model ensembles (Friedlingstein et al., 2022).

LPJ was run between January 1980 and July 2021 at a daily timestep and 0.5° resolution and was driven with MERRA2 reanalysis forcing (Gelaro et al., 2017; Zhang et al., 2018). The reanalysis data (total precipitation, 2-meter air temperature, downward shortwave radiation, and downward longwave radiation) were aggregated to a common daily time-step and downscaled to 0.5° spatial resolution grid using first order conservative interpolation. The LPJ-wsl state variables (i.e., carbon in vegetation, litter, and soils) were simulated to reach equilibrium by using a 1000-year spin-up with fire dynamics. Spin-up was completed using randomly selected climate inputs from 1980–2000 for MERRA2 with fixed atmospheric CO_2 to the 1860 value. After equilibrium, a transient simulation with fire effects and constant land cover was performed for the years 1980-2021, forced with changing climate conditions from MERRA2 reanalysis and varying atmospheric CO_2 concentration.

2.8 Step III: Cascade Analysis and Vegetation Anomaly Attribution

To investigate the potential for a temporal cascade through the Western US SPAC, AIRS humidity, AIRS temperature, AIRS VPD, GPM precipitation, SMAP soil moisture, SMAP VOD, GRACE TWS, and MODIS-based GPP time series were evaluated mainly between January 2020 and July 2021. We estimated the timing of anomalies across each variable as the month that each variable first becomes anomalous, or its z-score anomaly first deviates by more than one

standard deviation from the mean (|z-score|>1). Only months were considered that had z-score magnitudes consecutively greater than one before the maximum z-score anomaly. This step is similar to low pass filter methods by removing isolated anomalies due to noise. Furthermore, cross correlations were determined by computing the correlation between the variables at month offsets between -5 to 5 months of lag. For each pixel, we report the time lag of the maximum absolute correlation as well as the correlation at that time lag between each variable. Our method is objective in not specifying a search for positive or negative correlations only.

To attribute vegetation anomalies to features of environmental variable anomalies, we computed the maximum magnitude, spatial extent, and duration of anomalies within the SPAC in the Western US in 2020-2021. Specifically, the anomalies of each normalized variable in their available time series were sorted and ranked empirically. The extreme magnitude metric for each variable is the ranking of the most extreme normalized monthly anomaly between 2020-2021. For spatial extent, the same ranking procedure for each variable was repeated on a spatial extent metric: the areal extent of normalized z-scores below -1. Finally, the duration of anomalies below normalized z-scores of -1 between August 2020 and July 2021 were computed and compared against the mean anomaly durations from years before this period.

2.9: Step IV: Time Series Analysis using Causal Model

As a result of the cascade analysis, we used a causal model to test whether terrestrial water storage (TWS) has a causal influence on GPP across the region and whether direct influence of climate (within 1–3-month lags) drove large GPP deficits in 2021. Namely, Granger Causality (GC) tests (Granger, 1969) were chosen for this purpose. GC evaluates whether perturbations in one variable consistently result in future responses in another variable, a feature of causality. These perturbations need to influence the response variable beyond what can be predicted from the response variable's history. As such, GC relies on an autoregressive model:

$$GPP_t = \alpha + \sum_p \beta_{GPP} GPP_{t-p} + \beta_{TWS} TWS_{t-p} + \beta_{VPD} VPD_{t-p} + \beta_P P_{t-p} + \varepsilon_{t-p} \quad (2)$$

where p represents time lag (months). This equation is performed on the deseasonalized monthly anomalies of these variables between January 2003 and December 2019 to provide out of sample testing of the 2020-2021 study period. Seasonality was explicitly removed because it is known to spuriously inflate GC detection (Tuttle and Salvucci, 2017).

TWS, VPD, and P were selected to predict GPP based on the cascade analysis because of their known physical link to plant function, their observation availability, and length of time series, which are essential criteria for GC tests. A caveat is that P is meant to represent surface soil moisture here to isolate effects of deeper layer moisture sources from TWS. We do not directly use SMAP soil moisture due to its monthly sample size being too low for GC tests with SMAP retrievals being available after April 2015, while GPCP precipitation is available between 2003 and 2019. Monthly GPCP precipitation anomalies are correlated with SMAP soil moisture anomalies across the region (mean correlation of 0.53) between April 2015 and December 2020. Nevertheless, as a test, we repeated the analysis with SMAP soil moisture in place of GPCP precipitation in Eq. 2, but less confidence is placed in these results with a lower sample size. We also avoid reanalysis soil moisture products given their prescribed relationships with vegetation within their model frameworks.

Time lags (p) are optimized using quasi-information criterion. Statistical significance tests were performed in the GC framework by assessing the degree of residual sum of squares (RSS) inflation when leaving one target regressor (TWS, VPD, or P) out of the autoregressive model:

$$S = n\left(\frac{RSS_{Restricted} - RSS_{Full}}{RSS_{Full}}\right) \quad (3)$$

Here, n is number of observation pairs and the RSS of the unrestricted (full) model is compared to RSS of the restricted model with the target variable removed. The S statistic is chi-squared with lag number p as the degree of freedom. p-values less than 0.05 indicate that including a lagged variable such as TWS as an explanatory factor significantly increases the model's variance explained of GPP variations 1-3 months into the future. This would suggest TWS has a causal influence on GPP. Based on the cross-correlation analysis, we confirm that lags of 1-3 months are appropriate with GPP lagging P and VPD nearly identically by one month and TWS with only a one-month lag difference (Fig. S3). Despite the lag choice being the same across the variables in the autoregressive model by its construction, we don't anticipate inherent differences in lags between the predictors (P, VPD, TWS) creating biases given their one-month differences (Fig. S3) and the fact that repeating results with a constant lag of one month produces nearly identical results. Furthermore, as an independent test, we evaluate whether maximum rooting depths are deeper in Western US pixels where TWS Granger-causes GPP (based on Eq. 3) than pixels where TWS does not Granger-cause GPP.

We also used this causal model to explain why GPP anomalies were determined to be more negative in 2021 than in 2020 as "resilience tests". These tests used the Eq. 2 estimated parameter results from 2003-2019 to predict out-of-sample GPP anomalies in 2020-2021 using observed 2020-2021 inputs. We first tested if TWS is buffering GPP negative responses in 2020 by setting all 2020 TWS anomalies to the more negative TWS mean anomaly values between January and July 2021. TWS is buffering the GPP response in 2020 if the GPP model driven by more negative TWS anomaly inputs (from 2021) substantially lowers the GPP anomalies in 2020 compared to GPP anomalies driven by the baseline observed 2020 TWS anomalies. The analysis was performed on the pixels with statistically significant GC of TWS on GPP.

In "extreme amplification tests" to determine drivers of more negative GPP anomalies in 2021, we used Eq. 2 to determine whether GPP's typical response to land-atmosphere forcings (i.e., VPD, precipitation, TWS) between 2003-2019 would explain the magnitude of negative GPP response in 2021. If the model underestimates the magnitude of the observed negative GPP anomalies and there is evidence of prolonged SPAC dry anomalies carrying over between two years, this can partly indicate non-linear or compound effects (i.e., legacy effects) from prolonged anomalies in the SPAC. Namely, large deviations of Eq. 2 modeled GPP from observation-based FluxSat GPP would indicate effects other than linear response to the environment. In both tests, we further isolated the linear effect of the environment by removing the GPP autoregressive component ($\beta_{GPP} GPP_{t-p}$). We refer the reader to the SI for further discussion of the robustness of the GC method, resilience tests, and amplification tests.

3. Results and Discussion

3.1. Step I: Initial CO_2 Flux Anomaly Attribution

In June 2021 in the Western US, OCO-2 observed a +0.8 ppm XCO_2 anomaly (Fig. 2a), which co-occurred with large negative MODIS-based photosynthesis anomalies (Fig. 2b). The XCO_2 anomaly is not likely to be due to anomalously transported CO_2 from outside the region; the upwind Pacific Ocean had a negative XCO_2 anomaly at this time (Fig. 2a). As such, the June 2021 West US XCO_2 anomaly is an enhancement of +1.1 ppm above the background Pacific Ocean conditions, which is the largest anomaly in the available OCO-2 time series at three standard deviations above the mean. We estimate that this XCO_2 anomaly translates to a total CO_2 flux anomaly of 132±50 TgC/mo in June 2021 based on Eq. 1 (see Section 3.4). The

negative GPP anomaly in June 2021 is also about three standard deviations below the mean. Together, the satellite-based GPP and XCO_2 anomalies suggest a weakened Western US carbon uptake, likely due to decreased plant uptake of carbon.

Other flux components may not have been as much of a factor given that biomass burning emissions appeared to strengthen after July 2021 (Fig. 2c) and fossil fuel emissions were relatively constant (Fig. S1). Disturbance or land use change is not likely to be driving the results given there is not a step-change in GPP or XCO_2 observed in the anomaly time series. We acknowledge that ecosystem respiration anomalies may be partly driving the positive XCO_2 anomaly, but respiration is challenging to directly observe and its attribution within our framework is left for future work. Ultimately, these initial findings motivate quantifying the contribution of the biosphere anomalies to the 2021 carbon budget as well as identifying climatic drivers of ecosystem stress that at least partially drove positive atmospheric carbon concentration anomalies.

3.2 Step II: Climate Anomaly Detection

The Western US experienced high VPD and low soil moisture conditions beyond one standard deviation beginning in early 2020 and continuing into 2021 (Figs. 2d and 2e). Some of the driest soil moisture anomalies occurred in Spring 2021 before appearing to recover with rewetting by July 2021. VPD anomalies were of high magnitude in both summer 2020 and spring 2021. As such, we further attribute the carbon flux anomalies initially to climate-driven plant stress, given concurrent hot and dry anomalies (Figs. 2d and 2e) and photosynthesis anomalies (Fig. 2d). Based on the timing and spatial extent of these anomalies, we define this West US domain and January 2020 to July 2021 as the study domain for the remainder of the analysis.

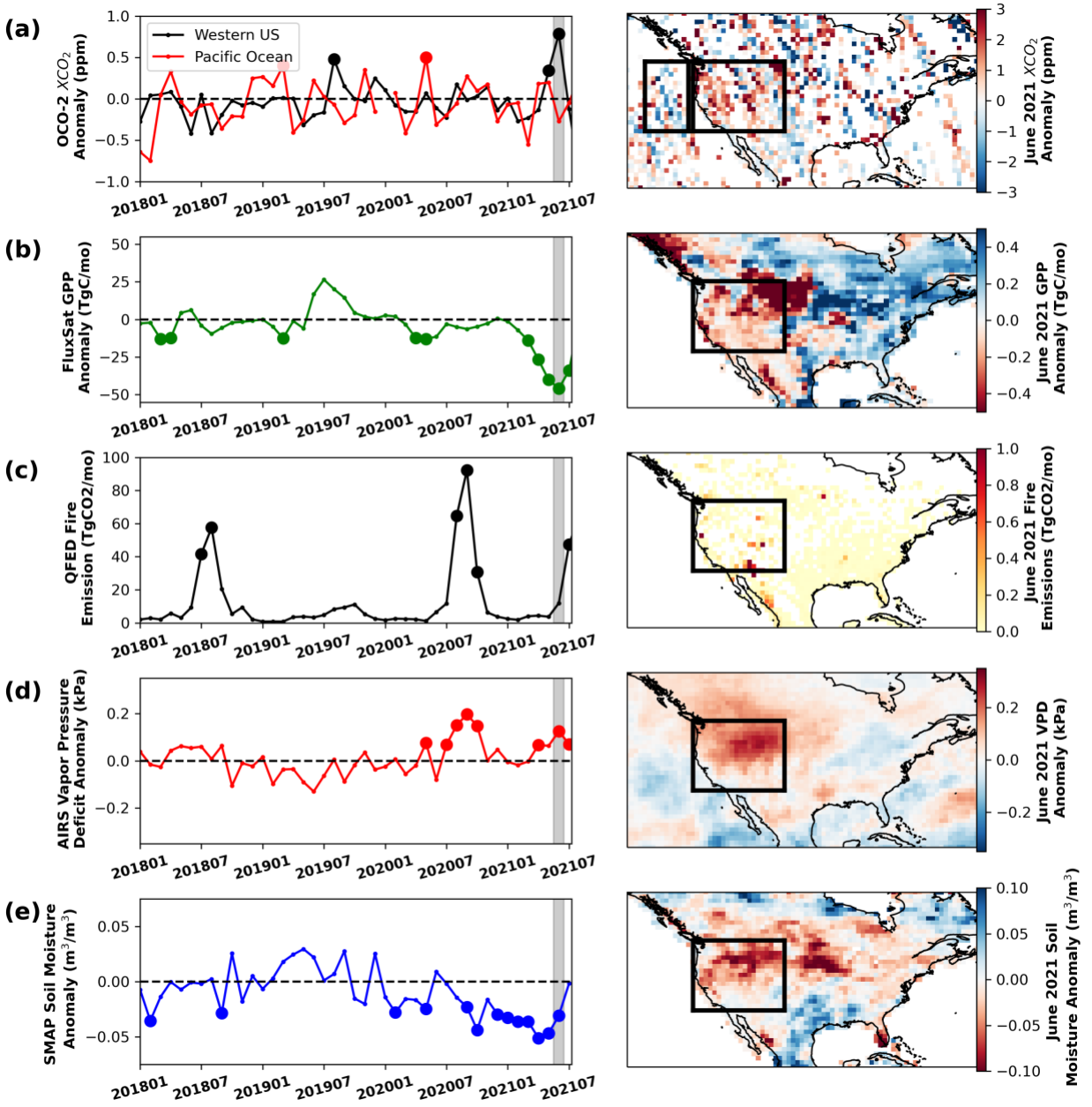

Fig. 2. Observations indicate large CO_2 flux anomalies in the Western US in spring 2021 originating mainly from water-stressed photosynthesis. Step I includes CO_2 flux anomaly detection from (A) OCO-2 XCO_2 column (CO_2) anomalies (ppm) with components from (B) MODIS-based FluxSat GPP anomalies and (C) QFED fire emissions. Step II includes identification of climatic anomalies from (D) AIRS vapor pressure deficit and (E) SMAP soil moisture anomalies. Time series are shown between January 2018 to July 2021. Larger dot symbols are those that exceed a one standard deviation anomaly for the region. June 2021 is shaded in the left column and shown spatially on right column. Time series plots exclude Pacific Ocean pixels.

3.3 Dynamic global vegetation model run

We use the LPJ DGVM as a reference to assess the value of integrated, low-latency satellite observations as well as the workflow's ability to inform DGVMs. LPJ agrees with our attribution in Fig. 2 that a large negative carbon flux anomaly from the biosphere occurred in spring 2021 (Fig. 3). Between January 1st and July 31st, 2021, the model simulates a cumulative NBP of -191 TgC. Since the 1980-2020 NBP average in this time range is 134 TgC (±123), this translates to a cumulative NBP anomaly of -320 TgC between January 1st and July 31st. Photosynthesis deficits made a large contribution to this negative CO_2 uptake anomaly where LPJ simulates a cumulative GPP anomaly of -480TgC between January 1st and July 31st (Fig. 3d).

This carbon flux anomaly is similar in magnitude to that of the drought and wildfire event in Australia in 2019-2020 (Byrne et al., 2021) and about half of that of the severe 2003 Europe drought (Ciais et al., 2005). Therefore, given a global annual terrestrial carbon sink of 2-3 PgC/yr (Friedlingstein et al., 2021), these Western US 2021 NBP anomaly magnitudes are equivalent to 10-15% of the global terrestrial sink and thus the event potentially presents such large carbon loss if cumulative NBP remains relatively constant beyond August as it has in previous years in this region. This LPJ implementation further motivates understanding water-limited regions characterized by low mean annual uptake, but large interannual variability (Ahlström et al., 2015; Poulter et al., 2014). Specifically, the Western US biosphere's annual mean carbon uptake has a relatively low contribution to the mean annual global terrestrial carbon uptake (<2%). However, the Western US biosphere's high sensitivity to climate variability results in a high variance of its annual mean uptake; LPJ simulates that the Western US is a carbon source in approximately one third of years and appears prone to large carbon efflux extremes that perturb the mean annual global carbon budget as in cases like 2021.

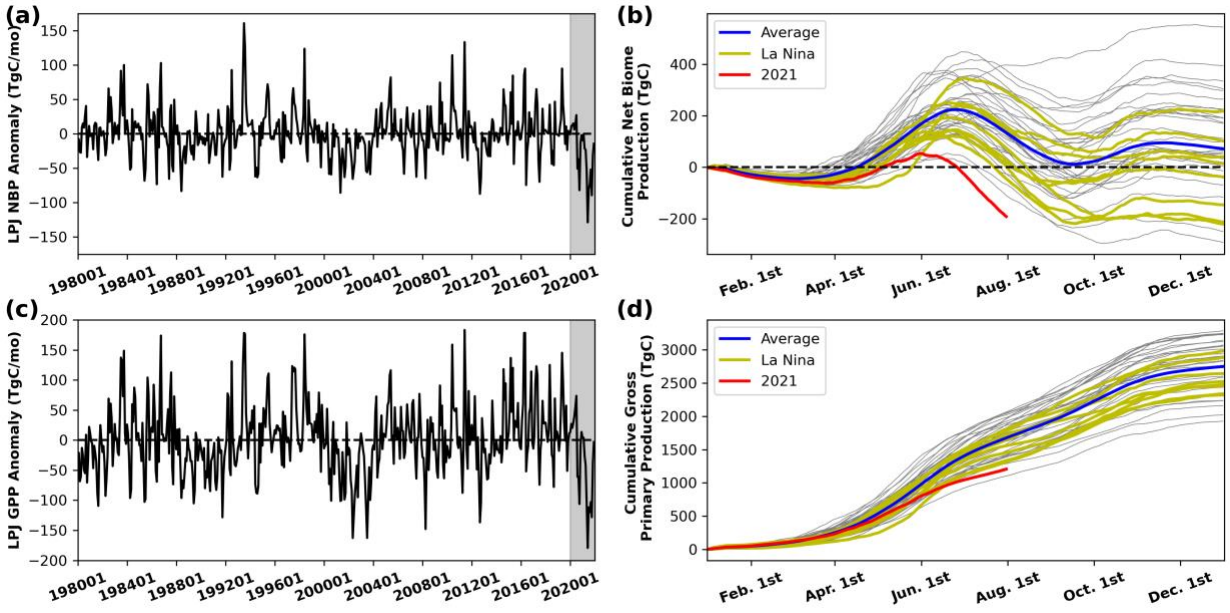

Fig. 3. LPJ model outputs of net biome production and gross primary production show biosphere carbon effluxes in 2021 in the Western US. (A and C) Monthly anomalies and (B and D) annual cumulative fluxes for each year beginning January 1st for both NBP and GPP. Gray lines in B and D show cumulative NBP or GPP for each year in the 1980-2021 range. La Nina years based on the Southern Oscillation Index which result in suppressed monsoon rainfall in the region are highlighted for comparison.

3.4 Greenhouse-gas satellites can detect and roughly estimate carbon cycle response to extreme biosphere anomalies

Despite satellite XCO_2 retrieval noise and various contributions to XCO_2, the Western US satellite XCO_2 anomalies are consistently correlated with surface carbon flux anomalies, especially natural GPP and NBP sources (Figs. 4a and 4b). This is in part due to the consistent advection from the Pacific Ocean into the Western US (Feldman et al., 2023). This coupling gives credence to detection of a large CO_2 flux with an extreme XCO_2 anomaly.

We quantify extreme CO_2 effluxes during Spring 2021 using XCO_2 anomalies and Eq. 1 to estimate their magnitudes. We estimate an anomaly CO_2 flux of 132±50 TgC/mo during June 2021 (Fig. 4c), when GPP anomalies are most negative (Fig. 2b). This compares with the LPJ-based estimate of 145 TgC/mo. Similarly, in March 2021, the OCO-2 mass balance estimate is 61±57 TgC/mo, while the LPJ+QFED estimate is 56 TgC/mo. There is disagreement between OCO-2 XCO_2 and LPJ flux estimates during 2020, a year we find that LPJ NBP may have overestimated efflux responses (see Section 3.6). Nevertheless, the overall correlation between the LPJ NBP reference and XCO_2 estimated surface fluxes has a magnitude 0.31, which highlights limitations using the flux estimation for nominal flux conditions as well as emphasizes the large uncertainty of each estimate. Tests with CarbonTracker show that the correlation improves to 0.55 without instrument noise, suggesting increased utility with improvements to XCO_2 sampling.

Fig. 4 suggests that there are opportunities to use XCO_2 satellite retrievals directly to augment Step I in rapidly detecting the monthly timing of surface carbon cycle anomalies. The rapid mass balance flux estimation methods have been developed and tested previously (Buchwitz et al., 2017; Feldman et al., 2023; Pandey et al., 2021). However, we emphasize limitations originating from atmospheric transport (Basu et al., 2018), simplistic assumptions of the mass balance approach (Varon et al., 2018), and OCO-2 instrument noise (Buchwitz et al., 2021). A recent investigation showed that these methods may only be used in regions with temporally consistent and unidirectional mean transport conditions, averaged over large enough areas, and under extreme surface flux conditions that place a CO_2 imprint on the atmosphere (Feldman et al., 2023). As such, these XCO_2 methods should be used in tandem with other datasets, and their lack of success does not hinder the overall framework.

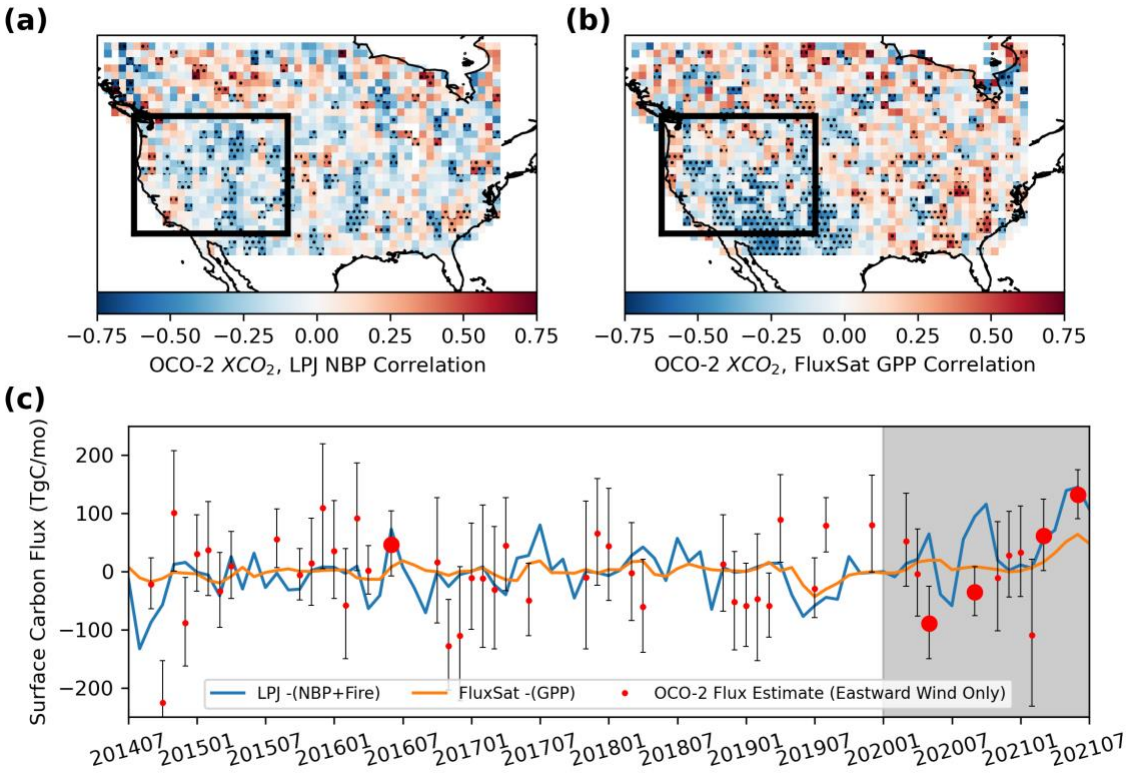

Fig. 4. Satellite retrieved XCO_2 provides an opportunity to evaluate extreme biosphere fluxes. (A and B): OCO-2 XCO_2 anomaly correlation with (A) LPJ NBP and (B) FluxSat GPP anomalies between June 2014 and July 2021. The Western US study region is delineated with black lines. Statistically significant correlations are stippled ($p<0.05$). (C) Flux estimates based on observed OCO-2 XCO_2 enhancements using XCO_2 anomalies in Fig. 2a and the mass balance in Eq. 1 plotted with biosphere flux anomalies from LPJ NBP and FluxSat GPP. Larger symbols are the cases of top five positive surface flux anomalies based on LPJ NBP + QFED (>85th percentile). Positive values are effluxes. The study period is highlighted in gray. Only months with a mainly eastward wind component are shown (<60^o and >-60^o, where 0^o is eastward). Error bars show 5th and 95th percentile uncertainty bounds.

3.5 Step III Cascade Analysis: Satellites observe an anomaly cascade through the soil-plant-atmosphere system

An anomaly cascade is evident from 2020 to 2021 where anomalous meteorological conditions (Figs 5a to 5d) precede land moisture anomalies (Figs. 5e to 5g), followed by photosynthesis anomalies (Fig. 5h and S2). The low latency, integrated satellite observations here thus initially attribute the large carbon efflux to plant water and heat stress. Specifically, the most negative photosynthesis anomalies in June 2021 can be qualitatively attributed to declines in soil moisture throughout 2020, TWS and VOD declines starting January 2021, and extreme VPD throughout the Western US that is partially due to the Pacific Northwest heatwave during spring 2021 (Philip et al., 2021). While VOD is a function of both dry biomass and plant saturation changes (Konings et al., 2021, 2019), we find that VOD anomalies tend to precede GPP anomalies (Figs. 5 and S2). Therefore, late 2020 VOD declines here likely indicate mainly

plant saturation loss rather than biomass loss given that loss of biomass would be concurrent with or follow photosynthetic losses (Rao et al., 2019). Additionally, although GPP showed declines in 2020 especially in the Southeast part of the domain as previously investigated (Dannenberg et al., 2021), the GPP declines throughout the West US were three times greater on average in 2021 than in 2020 (Fig. 5h). In Step IV, we investigate why there is a large difference in GPP anomalies between 2021 and 2020 despite extreme dry and hot conditions in both years (see Section 3.6).

Cross correlations show a lagged coupling between all components of the SPAC, confirming that a dry/hot anomaly cascade nominally takes place from the atmosphere to the soil and then to plants (Fig. S3). However, while anomalies typically propagate through the SPAC over less than 4-month timescales in this region (Fig. S3), peak atmospheric, soil, and vegetation anomalies during this extreme event are spread across a longer period of 12 months (Figs. 5 and S3). This lengthening of lags suggests a difference in the dynamics of this extreme hot-dry cascade within the SPAC than for typical anomalies. For example, we note that while monthly soil moisture and VPD anomalies are coupled in this region across the available time series (Pearson's correlation = -0.61; $p<0.05$), they become uncoupled during this extreme event; VPD had more abrupt anomalies with recovery of atmospheric conditions on average during the 2020-2021 winter months while soil moisture had persisting anomalies that did not recover until later spring 2021 (Fig. 5).

We find that the large Western US negative GPP anomalies are attributable to the warm, dry anomalies' extreme spatial extent. Specifically, most atmosphere and land anomalies in 2021 had the most extreme spatial extent of moderate anomalies in their available time series (Fig. 6b). However, the most extreme individual monthly magnitudes tended to be ranked in the top ten of their respective available time series, but not first (Fig. 6a). An exception is the maximum VPD anomalies that were the highest in their time series (Fig. 6a), but their timing primarily in 2020 may have only indirectly influenced 2021 GPP anomalies. Furthermore, anomaly durations were only 1-3 months longer than average years (Fig. 6c), with anomalies confined to specific months in summer 2020 and spring 2021. These findings are consistent with expectations that the spatial extent of terrestrial biosphere extremes, over extreme magnitude in a given month or their duration, will make the largest contributions to perturbing the global carbon cycle (Reichstein et al., 2013).

Cascades and their propagation are a common feature of hydrologic anomalies (Farahmand et al., 2021; Mukherjee et al., 2023), though their connection to the biosphere has not been investigated. We note that biosphere cascades are readily observed in other global locations and time periods (Figs. S4 and S5).

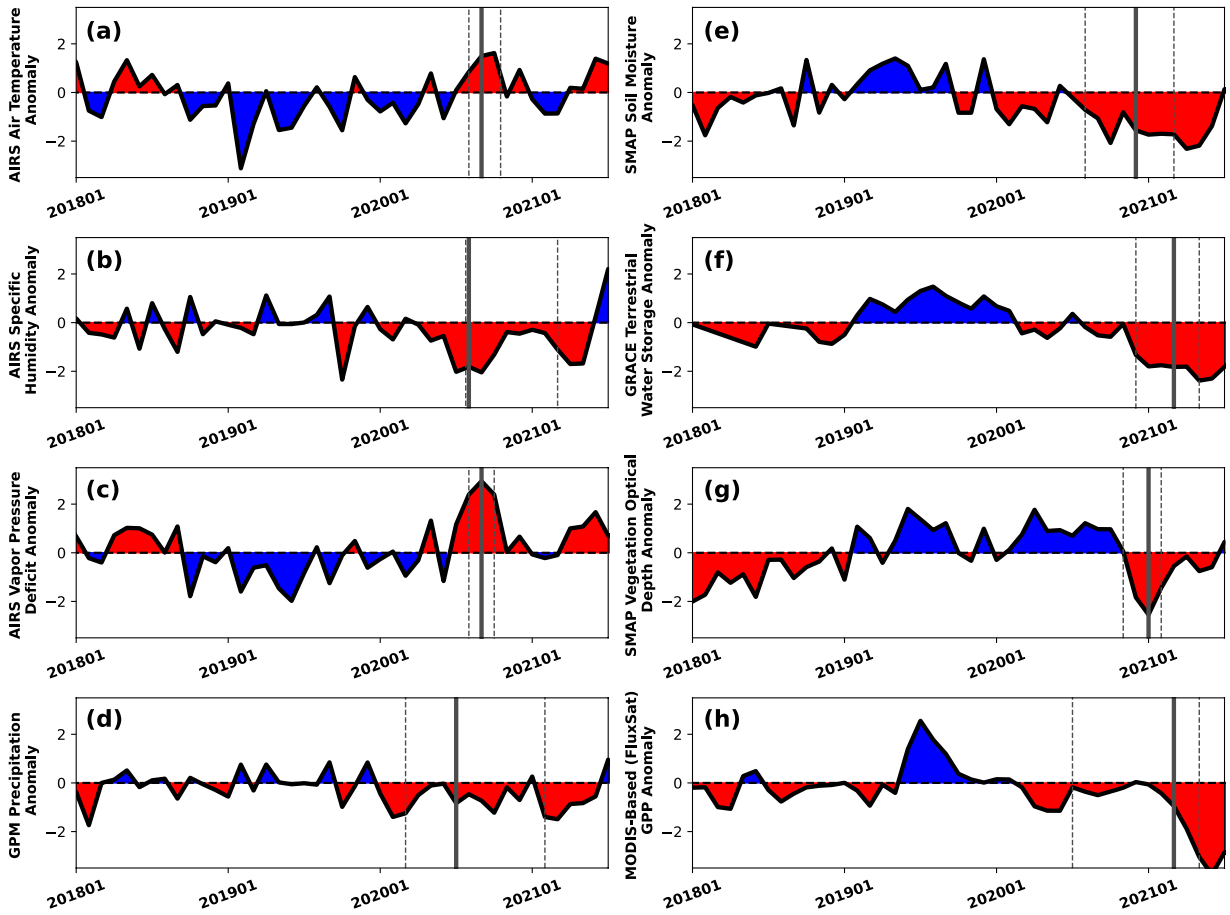

Fig. 5. A dry, hot anomaly propagation through the Western US soil-plant-atmosphere continuum is observed from Earth-observing satellite remote sensing platforms. Anomaly time series of atmospheric, soil, and biosphere factors averaged in the Western US region: (A) AIRS air temperature, (B) AIRS specific humidity, (C) AIRS vapor pressure deficit, (D) GPM precipitation, (E) SMAP soil moisture, (F) GRACE terrestrial water storage, (G) SMAP vegetation optical depth (vegetation water content), (H) MODIS-based FluxSat gross primary production. Values are normalized by subtracting their mean monthly climatology and dividing by their standard deviations. Vertical lines denote the initial timing of the warm/dry anomaly of each variable across the pixels in the study region with the solid line denoting median initial timing and dashed lines denoting the 25th and 75th percentiles.

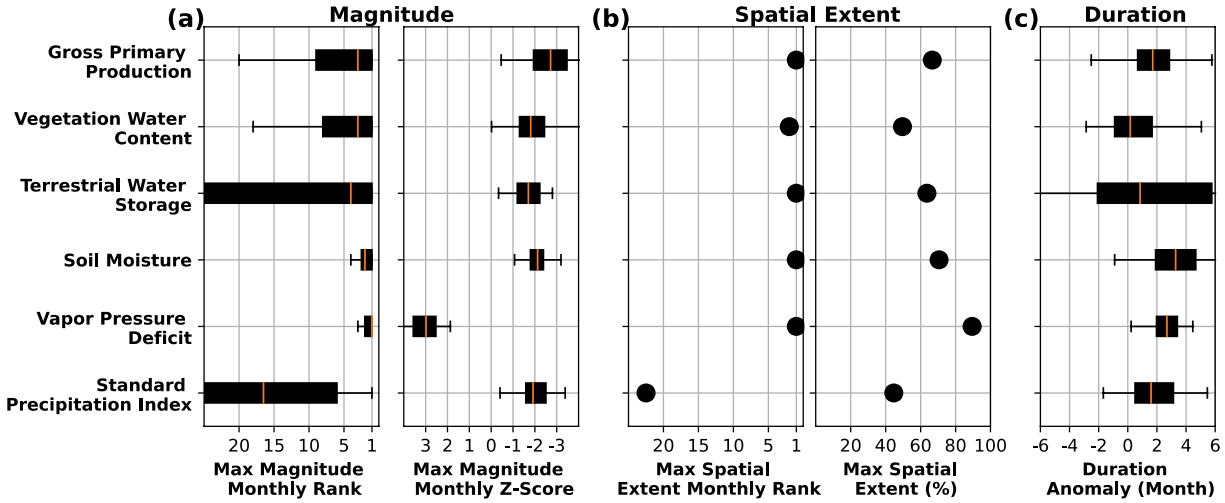

Fig. 6. The Western US atmosphere and land anomalies appear most characterized by an extreme spatial extent. (A) Maximum monthly anomaly magnitude. (B) Maximum monthly spatial extent of anomaly in the region based on percentage of the West US region that has a z-score less than -1 (above 1 for VPD). (C) Duration of the anomaly estimated as the number of consecutive months the respective z-score was less than -1 between August 2020 and July 2021 relative to anomaly durations in previous years. All plots share the same y-axis. The rank is based on high to low sorting of the monthly values in the time series where higher values indicate the largest respective dry or hot metric in the available time series occurred between between August 2020 and July 2021. Results are based on the empirical probability distributions of the monthly anomalies for the available time series ranging between years 2000 and 2021. Boxplots are the distribution of values from individual pixels within the Western US.

3.6 Step IV Causality Test: Western US biosphere response driven by connection to deeper soil moisture and amplification effects

The cascade analysis motivates a more specific investigation into why negative photosynthetic anomalies were larger in 2021 than in 2020 despite similar atmospheric forcing (Fig. 5). We find that the resilience conveyed by terrestrial water storage in 2020 to GPP as well as the compounding negative effects in 2021 partly drove the differing GPP responses between 2020 and 2021 (Fig. 7).

We find that terrestrial water storage Granger-causes GPP in 22% of the region over 1–3-month timescales, increasing to 32% in spring and summer (Fig. 7a). Note that this result is based on our GC model (Eq. 2) which adequately fits the observations in these regions with TWS Granger-causal influence with an average R^2 of 0.60 over all months and 0.69 during the spring and summer months. These model fits are high considering the removal of the seasonal cycle as well as use of mainly satellite observation datasets that inherently include noise. A potential source of uncertainty in the GC model is that GPCP precipitation anomalies were used to isolate the effects of plant-available surface soil moisture, due to SMAP soil moisture having too short of a monthly time series for data length requirements of the GC tests. However, despite the low sample size, repeating the analysis with SMAP soil moisture in place of precipitation results in an even higher area of the West US showing TWS Granger-causal influence on GPP providing more confidence in the results (Fig. S6). SMAP soil moisture significantly Granger-caused GPP in 58% of the region, which is not substantially more than GPCP precipitation which explained 50% of the region's GPP variations. There is too low of a sample size to assess spring

and summer months when using SMAP (Fig. S6). As such, use of GPCP precipitation instead of observed soil moisture does not appear to confound the result that TWS partially drives GPP in the region in addition to surface moisture.

Based on these GC results, we conclude that maintained TWS offered GPP resilience in 2020, but negative TWS anomalies in 2021 partly drove GPP declines. This suggests plant access to deeper soil moisture because TWS has been shown to represent intermediate-to-deep level soil moisture above the water table (Rodell and Famiglietti, 2001). Indeed, in the pixels where TWS Granger-causes GPP, we find that previously estimated maximum rooting depths (Fan et al., 2017) are deeper by 0.55m than in pixels where the causality is not detected ($p<0.05$ based on student t-test of means). Additionally, several recent studies confirm plant water use of deeper soil stores across the Western US, especially along the west coast (Kannenberg et al., 2023; McCormick et al., 2021; Miguez-Macho and Fan, 2021; Stocker et al., 2023). As a result, despite similar rainfall deficits between 2020 and 2021, maintained TWS in 2020 resulted in smaller negative GPP anomalies throughout 2020; if TWS anomalies in 2020 were set to those in 2021, the negative GPP anomalies in 2020 would have at least doubled (Fig. 7b). Maintained vegetation water status despite negative surface soil moisture anomalies in 2020 gives additional evidence for this finding (Fig. 5g). Nevertheless, there was a gradual, prolonged depletion of deeper soil stores between 2020 and 2021 with continued deficits in precipitation forcing, similarly to TWS dynamics during the 2018-2019 Europe drought (Boergens et al., 2020). Therefore, the large negative TWS anomalies in 2021 at least partially drove the spring 2021 negative GPP anomalies. In this case, deeper moisture sources were no longer able to offer resilience to GPP with moisture losses observed throughout the soil column in both surface soil moisture and TWS in 2021.

The causal model also shows that GPP's direct response to environmental conditions (VPD, precipitation, deeper soil moisture) within the previous 1-3 months are insufficient to explain the extreme negative GPP anomalies in Spring 2021, suggesting a nonlinear change of plant behavior due to persisting climatic effects (Fig. 7c). Namely, the causal model captures the observation-based GPP response to the environment before and throughout 2020, but cannot fully explain the largest negative GPP anomaly in spring 2021 using only 1-3 month lagged climatic anomalies (Fig. 7c). This is especially the case after removing the autoregressive component of GPP in Eq. 2 ($\beta_{GPP} GPP_{t-p}$), which represents the 1–3-month persistence of GPP and indirectly integrates longer-term biospheric memory responses (Fig. 7c; "Extreme Amplification Test 2"). Even with this lagged memory incorporated, which is expected to best explain the observations, the peak negative GPP anomaly magnitude in Spring 2021 is underestimated (Fig. 7c; "Extreme Amplification Test 1"), supporting presence of a nonlinear interactive or compounding effect not observed in the available time series. This test was performed in pixels that should result in the most negative GPP anomalies: pixels where TWS Granger-causes GPP that coincidentally also have more negative TWS deficits (Fig. S7). The exacerbated 2021 GPP anomalies may have been due to legacy effects of persisting climatic anomalies over multiple seasons and years starting in 2020 (Anderegg et al., 2020, 2015; A Bastos et al., 2020; Wolf et al., 2016) with little time for biosphere recovery (Schwalm et al., 2017; Werner et al., 2021), amplifying effects of land-atmosphere feedbacks on the biosphere (Feldman et al., 2020; Miralles et al., 2014; Zhou et al., 2019), and/or anomaly timing during plant-active phenological stages (Felton and Goldsmith, 2023).

LPJ modeled GPP anomalies do not show as large of a difference between 2020 and 2021 as that observed, suggesting the DGVM's lack of connection of GPP to intermediate-to-deeper

soil stores and/or inability to capture multi-year or multi-season legacy effects (Fig. 8). LPJ GPP negative anomalies in 2021 were 1.7 times higher than the 2020 GPP deficits. However, observation-based FluxSat GPP and OCO-2 SIF 2021 negative anomalies were 2.4 and 3.3 times their 2020 negative anomalies, respectively (Fig. 8), where SIF is discussed as a proxy for GPP here (Smith et al., 2018). We suspect the LPJ biosphere model potentially overestimated GPP loss in 2020 because of too high of biosphere sensitivity to surface soil moisture deficits, as has been found previously in DGVMs in water-limited regions (De Kauwe et al., 2015; Fisher et al., 2007). Due to interactive or compounding effects detected in the observations (Fig. 7c), LPJ may have also underestimated the negative GPP response in Spring 2021.

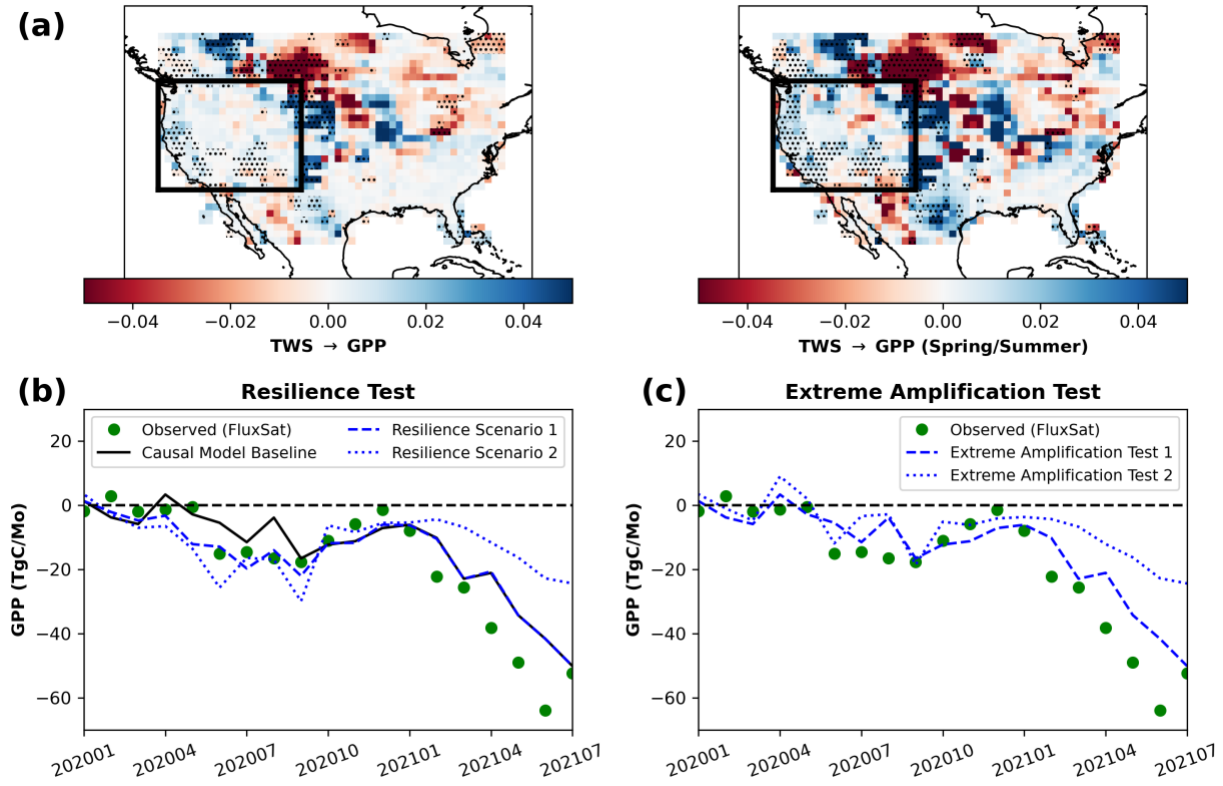

Fig. 7. GPP has a Granger-causal (GC) connection to deeper moisture sources in portions of the Western US. (A) Maps of Granger-causal influence of GRACE TWS on GPP. Values are regression coefficients (Eq. 2) with stippling indicating GC statistical significance ($p<0.05$), for all months and only spring/summer (April to September). (B) Tests for GPP resilience in 2020 from TWS. Lower predicted GPP anomalies in Scenarios 1 and 2 in 2020 than that of the baseline indicates GPP resilience conferred by deeper moisture. “Causal Model Baseline” is the null case demonstrating fit of the autoregressive model in Eq. 2 to the satellite based GPP. “Resilience Scenario 1” is the same as the null case but replacing TWS values in 2020 with the more negative 2021 TWS values. (C) Tests for effects other than direct climate influences on GPP in 2021. Less negative GPP anomalies predicted in the amplification tests than in satellite based GPP suggest an inability of 1-3 month lagged climate influences to explain the 2021 GPP anomalies. “Extreme Amplification Test 1” is the fit of the Eq. 2 linear model to GPP. In (B) and (C), the second scenario is the same as the first scenario but removes the autoregressive

component of GPP to isolate direct, linear effects of the environment on GPP. Tests are conducted only in pixels where GC is detected.

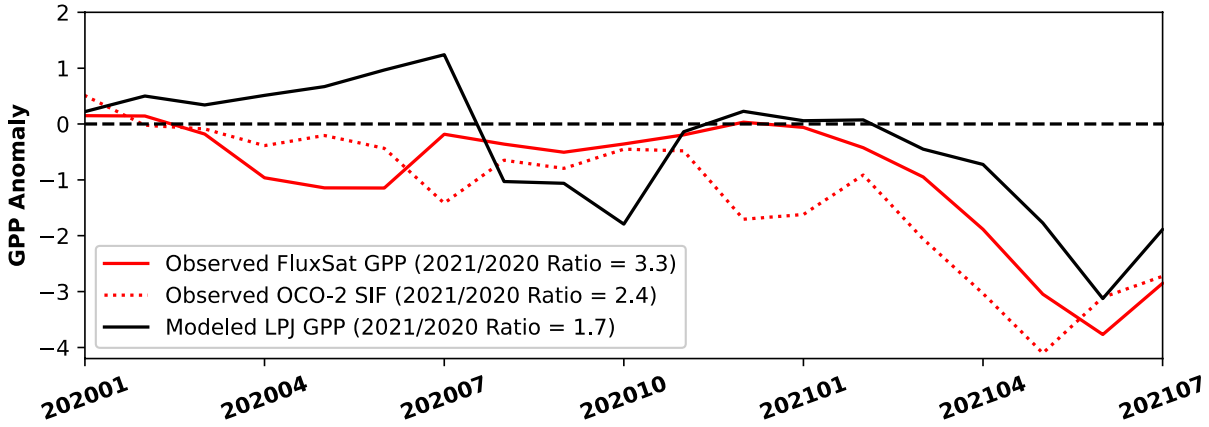

Fig. 8. Modeled versus observed GPP anomalies during the 2020-2021 Western US event. Time series are in the same z-score format as in Fig. 5. The "2021/2020 ratio" values reported in the legend are the most negative GPP or SIF anomaly magnitude between January and July 2021 divided by the most negative GPP or SIF anomaly magnitude between June and December 2020.

4. Conclusions

With increasing frequency and intensity of droughts and heatwaves and their complex impacts on terrestrial biosphere responses, it is becoming more important to observe, understand, and predict biosphere responses to extremes, especially at low latency (Reichstein et al., 2013). Detection and estimation of extreme carbon-climate feedbacks is also essential with an increasing need to monitor and partition anthropogenic and natural carbon fluxes. We demonstrate a low-latency workflow to evaluate biosphere response to extreme events using multiple satellite observations. Namely, it involves detecting carbon cycle anomalies and associated climate anomalies, conducting a cascade analysis to pinpoint specific environmental drivers of the anomaly, and conducting a time series analysis to establish more specific linkages between variables informed from the previous steps. The workflow and analysis is more detailed compared to global attributions (Mukherjee et al., 2023; Yang et al., 2023) in order to evaluate complex sub-seasonal interactions between a breadth of climate variables and terrestrial biosphere variables. These interactions might change substantially in time and space. We focus on an extreme 2020-2021 event in the Western US, which is a hotspot for projected increased frequency and intensity of droughts (Cook et al., 2021) that will translate to terrestrial biosphere responses because of the region's strong water-carbon cycle coupling (Short Gianotti et al., 2019).

We show how satellite-based photosynthesis and atmospheric carbon concentration anomalies can be used to attribute carbon anomalies to biosphere stress and, in some cases, roughly estimate large CO_2 flux anomalies. Furthermore, our cascade analysis demonstrates how the constellation of remote sensing platforms can attribute biosphere anomalies to detailed environmental features. We then use the cascade analysis to demonstrate the importance of the extreme anomaly spatial extent rather than magnitude or duration, negative photosynthesis anomaly amplification due to potential legacy effects, and biosphere resilience likely due to plant connection to deeper soil moisture in some regions of the West US. Finally, global models (ESMs, DGVMs) tend to have challenges characterizing the terrestrial biosphere response to

extremes and we show that such an observational framework at the spatiotemporal scales of these models presents an independent testbed for modeling drought response mechanisms. For example, we find here that the LPJ biosphere model may have overestimated photosynthesis negative anomalies in 2020 and/or underestimated negative anomalies in 2021.

We ultimately recommend that detailed observation-based case studies such as this are conducted on drought and heatwave events to understand biosphere responses to extremes, which are not typically predictable from nominal ecosystem function. As such, these observation-based studies can inform model representation of biosphere response to climatic extremes. The low-latency of the model workflow can also be used for rapid attribution applications.

Acknowledgements

Andrew F. Feldman's research was supported by an appointment to the NASA Postdoctoral Program at the NASA Goddard Space Flight Center, administered by Oak Ridge Associated Universities under contract with NASA. Research conducted by Abhishek Chatterjee was carried out at the Jet Propulsion Laboratory, California Institute of Technology, under a contract with the National Aeronautics and Space Administration (80NM0018D0004) and through grant number 80NSSC20K0006. The authors thank the editor and anonymous reviewers for helpful comments which improved the manuscript.

Data Availability

The data that support the findings of this study are openly available in Zenodo at 10.5281/zenodo.7825590. These data were derived from resources available in the public domain including OCO-2 data (https://disc.gsfc.nasa.gov), GRACE data (https://grace.jpl.nasa.gov), AIRS data (https://disc.gsfc.nasa.gov), QFED outputs (https://disc.gsfc.nasa.gov), SMAP-based MT-DCA data (https://doi.org/10.5281/zenodo.5579549), FluxSat data (https://daac.ornl.gov/), GPCP data (https://psl.noaa.gov/data/gridded/data.gpcp.html), CarbonTracker data (https://gml.noaa.gov/ccgg/carbontracker/), MERRA2 data (https://disc.gsfc.nasa.gov), and Carbon Monitor data (https://carbonmonitor.org).

References

Adler, R.F., Huffman, G.J., Chang, A., Ferraro, R., Xie, P.P., Janowiak, J., Rudolf, B., Schneider, U., Curtis, S., Bolvin, D., Gruber, A., Susskind, J., Arkin, P., Nelkin, E., 2003. The version-2 global precipitation climatology project (GPCP) monthly precipitation analysis (1979-present). J. Hydrometeorol. 4, 1147–1167. https://doi.org/10.1175/1525-7541(2003)004<1147:TVGPCP>2.0.CO;2

Ahlström, A., Raupach, M.R., Schurgers, G., Smith, B., Arneth, A., Jung, M., Reichstein, M., Canadell, J.G., Friedlingstein, P., Jain, A.K., Kato, E., Poulter, B., Sitch, S., Stocker, B.D., Viovy, N., Wang, Y.P., Wiltshire, A., Zaehle, S., Zeng, N., 2015. The dominant role of semi-arid ecosystems in the trend and variability of the land CO2 sink. Science (80-.). 348, 895–900. https://doi.org/10.1002/2015JA021022

Ainsworth, E.A., Long, S.P., 2005. What have we learned from 15 years of free-air CO2 enrichment (FACE)? A meta-analytic review of the responses of photosynthesis, canopy properties and plant production to rising CO2. New Phytol. https://doi.org/10.1111/j.1469-8137.2004.01224.x

Anderegg, W.R.L., Schwalm, C., Biondi, F., Camarero, J.J., Koch, G., Litvak, M., Ogle, K.,

Shaw, J.D., Shevliakova, E., Williams, A.P., Wolf, A., Ziaco, E., Pacala, S., 2015. Pervasive drought legacies in forest ecosystems and their implications for carbon cycle models. Science (80-.). 349, 528–532. https://doi.org/10.1126/science.aab1833

Anderegg, W.R.L., Trugman, A.T., Badgley, G., Konings, A.G., Shaw, J., 2020. Divergent forest sensitivity to repeated extreme droughts. Nat. Clim. Chang. 10, 1091–1095. https://doi.org/10.1038/s41558-020-00919-1

Bastos, A, Ciais, P., Friedlingstein, P., Sitch, S., Pongratz, J., Fan, L., Wigneron, J.P., Weber, U., Reichstein, M., Fu, Z., Anthoni, P., Arneth, A., Haverd, V., Jain, A.K., Joetzjer, E., 2020. Direct and seasonal legacy effects of the 2018 heat wave and drought on European ecosystem productivity. Sci. Adv. 6, 1–14.

Bastos, A., Ciais, P., Friedlingstein, P., Sitch, S., Pongratz, J., Fan, L., Wigneron, J.P., Weber, U., Reichstein, M., Fu, Z., Anthoni, P., Arneth, A., Haverd, V., Jain, A.K., Joetzjer, E., Knauer, J., Lienert, S., Loughran, T., McGuire, P.C., Tian, H., Viovy, N., Zaehle, S., 2020. Direct and seasonal legacy effects of the 2018 heat wave and drought on European ecosystem productivity. Sci. Adv. 6, 1–14. https://doi.org/10.1126/sciadv.aba2724

Bastos, A., Orth, R., Reichstein, M., Ciais, P., Viovy, N., Zaehle, S., Anthoni, P., Arneth, A., Gentine, P., Joetzjer, E., Lienert, S., Loughran, T., McGuire, P.C., Sungmin, O., Pongratz, J., Sitch, S., 2021. Vulnerability of European ecosystems to two compound dry and hot summers in 2018 and 2019. Earth Syst. Dyn. 12, 1015–1035. https://doi.org/10.5194/esd-12-1015-2021

Basu, S., Baker, D.F., Chevallier, F., Patra, P.K., Liu, J., Miller, J.B., 2018. The impact of transport model differences on CO2 surface flux estimates from OCO-2 retrievals of column average CO2. Atmos. Chem. Phys. 18, 7189–7215. https://doi.org/10.5194/acp-18-7189-2018

Boergens, E., Güntner, A., Dobslaw, H., Dahle, C., 2020. Quantifying the Central European Droughts in 2018 and 2019 With GRACE Follow-On. Geophys. Res. Lett. 47. https://doi.org/10.1029/2020GL087285

Buchwitz, M., Reuter, M., Noël, S., Bramstedt, K., Schneising, O., Hilker, M., Fuentes Andrade, B., Bovensmann, H., Burrows, J.P., Di Noia, A., Boesch, H., Wu, L., Landgraf, J., Aben, I., Retscher, C., O'Dell, C.W., Crisp, D., 2021. Can a regional-scale reduction of atmospheric CO2during the COVID-19 pandemic be detected from space? A case study for East China using satellite XCO2retrievals. Atmos. Meas. Tech. 14, 2141–2166. https://doi.org/10.5194/amt-14-2141-2021

Buchwitz, M., Schneising, O., Reuter, M., Heymann, J., Krautwurst, S., Bovensmann, H., Burrows, J.P., Boesch, H., Parker, R.J., Somkuti, P., Detmers, R.G., Hasekamp, O.P., Aben, I., Butz, A., Frankenberg, C., Turner, A.J., 2017. Satellite-derived methane hotspot emission estimates using a fast data-driven method. Atmos. Chem. Phys. 17, 5751–5774. https://doi.org/10.5194/acp-17-5751-2017

Byrne, B., Liu, J., Lee, M., Yin, Y., Bowman, K.W., Miyazaki, K., Norton, A.J., Joiner, J., Pollard, D.F., Griffith, D.W.T., Velazco, V.A., Deutscher, N.M., Jones, N.B., Paton-Walsh, C., 2021. The carbon cycle of southeast Australia during 2019–2020: Drought, fires, and subsequent recovery. AGU Adv. 2, e2021AV000469.

Chatterjee, A., Gierach, M.M., Sutton, A.J., Feely, R.A., Crisp, D., Eldering, A., Gunson, M.R., O'Dell, C.W., Stephens, B.B., Schimel, D.S., 2017. Influence of El Niño on atmospheric CO2 over the tropical Pacific Ocean: Findings from NASA's OCO-2 mission. Science (80-.). 358. https://doi.org/10.1126/science.aam5776

Chevallier, F., 2018. Comment on “Contrasting carbon cycle responses of the tropical continents to the 2015–2016 El Niño.” Science (80-.). 362, 1–3. https://doi.org/10.1126/science.aar5432

Ciais, P., Dolman, A.J., Bombelli, A., Duren, R., Peregon, A., Rayner, P.J., Miller, C., Gobron, N., Kinderman, G., Marland, G., Gruber, N., Chevallier, F., Andres, R.J., Balsamo, G., Bopp, L., Bréon, F.M., Broquet, G., Dargaville, R., Battin, T.J., Borges, A., Bovensmann, H., Buchwitz, M., Butler, J., Canadell, J.G., Cook, R.B., Defries, R., Engelen, R., Gurney, K.R., Heinze, C., Heimann, M., Held, A., Henry, M., Law, B., Luyssaert, S., Miller, J., Moriyama, T., Moulin, C., Myneni, R.B., Nussli, C., Obersteiner, M., Ojima, D., Pan, Y., Paris, J.D., Piao, S.L., Poulter, B., Plummer, S., Quegan, S., Raymond, P., Reichstein, M., Rivier, L., Sabine, C., Schimel, D., Tarasova, O., Valentini, R., Wang, R., Van Der Werf, G., Wickland, D., Williams, M., Zehner, C., 2014. Current systematic carbon-cycle observations and the need for implementing a policy-relevant carbon observing system. Biogeosciences 11, 3547–3602. https://doi.org/10.5194/bg-11-3547-2014

Ciais, P., Reichstein, M., Viovy, N., Granier, A., Ogée, J., Allard, V., Aubinet, M., Buchmann, N., Bernhofer, C., Carrara, A., Chevallier, F., De Noblet, N., Friend, A.D., Friedlingstein, P., Grünwald, T., Heinesch, B., Keronen, P., Knohl, A., Krinner, G., Loustau, D., Manca, G., Matteucci, G., Miglietta, F., Ourcival, J.M., Papale, D., Pilegaard, K., Rambal, S., Seufert, G., Soussana, J.F., Sanz, M.J., Schulze, E.D., Vesala, T., Valentini, R., 2005. Europe-wide reduction in primary productivity caused by the heat and drought in 2003. Nature 437, 529–533. https://doi.org/10.1038/nature03972

Cook, B.I., Mankin, J.S., Williams, A.P., Marvel, K.D., Smerdon, J.E., Liu, H., 2021. Uncertainties , Limits , and Benefits of Climate Change Mitigation for Soil Moisture Drought in Southwestern North America Earth ’ s Future. Earth’s Futur. 1–19.

Crisp, D., Atlas, R.M., Breon, F.M., Brown, L.R., Burrows, J.P., Ciais, P., Connor, B.J., Doney, S.C., Fung, I.Y., Jacob, D.J., Miller, C.E., O’Brien, D., Pawson, S., Randerson, J.T., Rayner, P., Salawitch, R.J., Sander, S.P., Sen, B., Stephens, G.L., Tans, P.P., Toon, G.C., Wennberg, P.O., Wofsy, S.C., Yung, Y.L., Kuang, Z., Chudasama, B., Sprague, G., Weiss, B., Pollock, R., Kenyon, D., Schroll, S., 2004. The Orbiting Carbon Observatory (OCO) mission. Adv. Sp. Res. 34, 700–709. https://doi.org/10.1016/j.asr.2003.08.062

Dannenberg, M.P., Smith, W.K., Zhang, Y., Song, C., Huntzinger, D.N., Moore, D.J.P., 2021. Large-Scale Reductions in Terrestrial Carbon Uptake Following Central Pacific El Niño. Geophys. Res. Lett. 48, 1–11. https://doi.org/10.1029/2020GL092367

Dannenberg, M.P., Yan, D., Barnes, M.L., Smith, W.K., Johnston, M.R., Scott, R.L., Biederman, J.A., Knowles, J.F., Wang, X., Duman, T., Litvak, M.E., Kimball, J.S., Williams, A.P., Zhang, Y., 2022. Exceptional heat and atmospheric dryness amplified losses of primary production during the 2020 U.S. Southwest hot drought. Glob. Chang. Biol. 1–13. https://doi.org/10.1111/gcb.16214

De Kauwe, M.G., Zhou, S.X., Medlyn, B.E., Pitman, A.J., Wang, Y.P., Duursma, R.A., Prentice, I.C., 2015. Do land surface models need to include differential plant species responses to drought? Examining model predictions across a mesic-xeric gradient in Europe. Biogeosciences 12, 7503–7518. https://doi.org/10.5194/bg-12-7503-2015

Egea, G., Verhoef, A., Vidale, P.L., 2011. Towards an improved and more flexible representation of water stress in coupled photosynthesis-stomatal conductance models. Agric. For. Meteorol. 151, 1370–1384. https://doi.org/10.1016/j.agrformet.2011.05.019

Fan, Y., Miguez-Macho, G., Jobbágy, E.G., Jackson, R.B., Otero-Casal, C., 2017. Hydrologic

regulation of plant rooting depth. Proc. Natl. Acad. Sci. U. S. A. 114, 10572–10577. https://doi.org/10.1073/pnas.1712381114

Farahmand, A., Reager, J.T., Madani, N., 2021. Drought Cascade in the Terrestrial Water Cycle: Evidence From Remote Sensing. Geophys. Res. Lett. 48, 1–10. https://doi.org/10.1029/2021GL093482

Feldman, A.F., Konings, A., Piles, M., Entekhabi, D., 2021. The Multi-Temporal Dual Channel Algorithm (MT-DCA) (Version 5) [Data set]. Zenodo. https://doi.org/https://doi.org/10.5281/zenodo.5619583

Feldman, A.F., Short Gianotti, D.J., Trigo, I.F., Salvucci, G.D., Entekhabi, D., 2020. Land-atmosphere drivers of landscape-scale plant water content loss. Geophys. Res. Lett. 47, e2020GL090331.

Feldman, A.F., Zhang, Z., Yoshida, Y., Chatterjee, A., Poulter, B., 2023. Using Orbiting Carbon Observatory-2 (OCO-2) column CO2 retrievals to rapidly detect and estimate biospheric surface carbon flux anomalies. Atmos. Chem. Phys. 23, 1545–1563.

Felton, A.J., Goldsmith, G.R., 2023. Timing and magnitude of drought impacts on carbon uptake across a grassland biome. Glob. Chang. Biol. 1–14. https://doi.org/10.1111/gcb.16637

Fisher, R.A., Williams, M., da Costa, A.L., Malhi, Y., da Costa, R.F., Almeida, S., Meir, P., 2007. The response of an Eastern Amazonian rain forest to drought stress: Results and modelling analyses from a throughfall exclusion experiment. Glob. Chang. Biol. 13, 2361–2378. https://doi.org/10.1111/j.1365-2486.2007.01417.x

Flach, M., Gans, F., Brenning, A., Denzler, J., Reichstein, M., Rodner, E., Bathiany, S., Bodesheim, P., Guanche, Y., Sippel, S., Mahecha, M.D., 2017. Multivariate anomaly detection for Earth observations: A comparison of algorithms and feature extraction techniques. Earth Syst. Dyn. 8, 677–696. https://doi.org/10.5194/esd-8-677-2017

Fountain, H., 2021. The Western Drought Is Bad. Here's What You Should Know About it. New York Times.

Frank, Dorothea, Reichstein, M., Bahn, M., Thonicke, K., Frank, David, Mahecha, M.D., Smith, P., van der Velde, M., Vicca, S., Babst, F., Beer, C., Buchmann, N., Canadell, J.G., Ciais, P., Cramer, W., Ibrom, A., Miglietta, F., Poulter, B., Rammig, A., Seneviratne, S.I., Walz, A., Wattenbach, M., Zavala, M.A., Zscheischler, J., 2015. Effects of climate extremes on the terrestrial carbon cycle: Concepts, processes and potential future impacts. Glob. Chang. Biol. 21, 2861–2880. https://doi.org/10.1111/gcb.12916

Friedlingstein, P., Jones, M.W., O'Sullivan, M., Al., E., 2021. Global Carbon Budget 2021. Earth Syst. Sci. Data Discuss.

Friedlingstein, P., Sullivan, M.O., Jones, M.W., Andrew, R.M., Gregor, L., Hauck, J., Quéré, C. Le, Luijkx, I.T., Olsen, A., Peters, G.P., Peters, W., 2022. Global Carbon Budget 2022. Earth Syst. Sci. Data 4811–4900.

Gelaro, R., McCarty, W., Suárez, M.J., Todling, R., Molod, A., Takacs, L., Randles, C.A., Darmenov, A., Bosilovich, M.G., Reichle, R., Wargan, K., Coy, L., Cullather, R., Draper, C., Akella, S., Buchard, V., Conaty, A., da Silva, A.M., Gu, W., Kim, G.K., Koster, R., Lucchesi, R., Merkova, D., Nielsen, J.E., Partyka, G., Pawson, S., Putman, W., Rienecker, M., Schubert, S.D., Sienkiewicz, M., Zhao, B., 2017. The modern-era retrospective analysis for research and applications, version 2 (MERRA-2). J. Clim. 30, 5419–5454. https://doi.org/10.1175/JCLI-D-16-0758.1

Granger, C.W.J., 1969. Investigating Causal Relations by Econometric Models and Cross-spectral Methods. Econometrica 37, 424–438.

Green, J.K., Konings, A.G., Alemohammad, S.H., Berry, J., Entekhabi, D., Kolassa, J., Lee, J.E., Gentine, P., 2017. Regionally strong feedbacks between the atmosphere and terrestrial biosphere. Nat. Geosci. 10, 410–414. https://doi.org/10.1038/ngeo2957

Green, J.K., Seneviratne, S.I., Berg, A.M., Findell, K.L., Hagemann, S., Lawrence, D.M., Gentine, P., 2019. Large influence of soil moisture on long-term terrestrial carbon uptake. Nature 565, 476–479. https://doi.org/10.1186/1750-0680-2-5

Grünzweig, J.M., Boeck, H.J. De, Rey, A., Santos, M.J., Adam, O., Bahn, M., Belnap, J., Deckmyn, G., Dekker, S.C., Flores, O., 2022. Ecosystem Functioning in a Drier and Warmer World. Nat. Ecol. Evol. 6.

Hakkarainen, J., Ialongo, I., Tamminen, J., 2016. Direct space-based observations of anthropogenic CO2 emission areas from OCO-2. Geophys. Res. Lett. 43, 11,400-11,406. https://doi.org/10.1002/2016GL070885

Haverd, V., Ahlström, A., Smith, B., Canadell, J.G., 2017. Carbon cycle responses of semi-arid ecosystems to positive asymmetry in rainfall. Glob. Chang. Biol. 23, 793–800. https://doi.org/10.1111/gcb.13412

Huffman, G.., Stocker, E.F., Bolvin, D.T., Nelkin, E.J., Tan, J., 2019. GPM IMERG Final Precipitation L3 Half Hourly 0.1 degree x 0.1 degree V06, Greenbelt, MD, Goddard Earth Sciences Data and Information Services Center (GES DISC), Accessed: [03.01.20.

Joiner, J., Yoshida, Y., 2021. Global MODIS and FLUXNET-derived Daily Gross Primary Production, V2. ORNL DAAC, Oak Ridge, Tennessee, USA. https://doi.org/10.3334/ORNLDAAC/1835.

Joiner, J., Yoshida, Y., 2020. Satellite-based reflectances capture large fraction of variability in global gross primary production (GPP) at weekly time scales. Agric. For. Meteorol. 291, 108092. https://doi.org/10.1016/j.agrformet.2020.108092

Kannenberg, S.A., Barnes, M.L., Bowling, D.R., Driscoll, A.W., Guo, J.S., Anderegg, W.R.L., 2023. Agricultural and Forest Meteorology Quantifying the drivers of ecosystem fluxes and water potential across the soil-plant-atmosphere continuum in an arid woodland. Agric. For. Meteorol. 329.

Keenan, T.F., Gray, J., Friedl, M.A., Toomey, M., Bohrer, G., Hollinger, D.Y., Munger, J.W., O'Keefe, J., Schmid, H.P., Wing, I.S., Yang, B., Richardson, A.D., 2014. Net carbon uptake has increased through warming-induced changes in temperate forest phenology. Nat. Clim. Chang. 4, 598–604. https://doi.org/10.1038/nclimate2253

Konings, A.G., Holtzman, N.M., Rao, K., Xu, L., Saatchi, S.S., 2021. Interannual Variations of Vegetation Optical Depth are Due to Both Water Stress and Biomass Changes. Geophys. Res. Lett. 48, 1–9. https://doi.org/10.1029/2021GL095267

Konings, A.G., Rao, K., Steele-Dunne, S.C., 2019. Macro to micro: microwave remote sensing of plant water content for physiology and ecology. New Phytol. 223, 1166–1172. https://doi.org/10.1111/nph.15808

Körner, C., 2003. Slow in , Rapid out : Carbon Flux Studies and Kyoto Targets Published by : American Association for the Advancement of Science. Science (80-.). 300, 1242–1243.

Koster, R.D., Darmenov, A., Silva, A., 2015. The Quick Fire Emissions Dataset (QFED): Documentation of Versions 2.1, 2.2 and 2.4. Volume 38; Technical Report Series on Global Modeling and Data Assimilation.

Liu, J., Bowman, K.W., Schimel, D.S., Parazoo, N.C., Jiang, Z., Lee, M., Bloom, A.A., Wunch, D., Frankenberg, C., Sun, Y., O'Dell, C.W., Gurney, K.R., Menemenlis, D., Gierach, M., Crisp, D., Eldering, A., 2017. Contrasting carbon cycle responses of the tropical continents

to the 2015–2016 El Niño. Science (80-.). 358. https://doi.org/10.1126/science.aam5690
Liu, M., van der A, R., van Weele, M., Eskes, H., Lu, X., Veefkind, P., de Laat, J., Kong, H., Wang, J., Sun, J., Ding, J., Zhao, Y., Weng, H., 2021. A New Divergence Method to Quantify Methane Emissions Using Observations of Sentinel-5P TROPOMI. Geophys. Res. Lett. 48, 1–10. https://doi.org/10.1029/2021GL094151
Liu, Z., Ciais, P., Deng, Z., Lei, R., Davis, S.J., Feng, S., Zheng, B., 2020. Near-real-time monitoring of global CO 2 emissions reveals the effects of the COVID-19 pandemic. Nat. Commun. 11.
Luo, X., Keenan, T.F., 2022. Tropical extreme droughts drive long-term increase in atmospheric CO2 growth rate variability. Nat. Commun. 13, 1–10. https://doi.org/10.1038/s41467-022-28824-5
McCormick, E.L., Dralle, D.N., Hahm, W.J., Tune, A.K., Schmidt, L.M., Chadwick, K.D., Rempe, D.M., 2021. Widespread woody plant use of water stored in bedrock. Nature 597, 225–229. https://doi.org/10.1038/s41586-021-03761-3
Mckee, T.B., Doesken, N.J., Kleist, J., 1993. The relationship of drought frequency and duration to time scales. AMS 8th Conf. Appl. Climatol. 179–184. https://doi.org/citeulike-article-id:10490403
Meroni, M., Fasbender, D., Rembold, F., Atzberger, C., Klisch, A., 2019. Near real-time vegetation anomaly detection with MODIS NDVI: Timeliness vs. accuracy and effect of anomaly computation options. Remote Sens. Environ. 221, 508–521. https://doi.org/10.1016/j.rse.2018.11.041
Miguez-Macho, G., Fan, Y., 2021. Spatiotemporal origin of soil water taken up by vegetation. Nature.
Miralles, D.G., Teuling, A.J., Van Heerwaarden, C.C., De Arellano, J.V.G., 2014. Mega-heatwave temperatures due to combined soil desiccation and atmospheric heat accumulation. Nat. Geosci. 7, 345–349. https://doi.org/10.1038/ngeo2141
Mukherjee, S., Mishra, A.K., Zscheischler, J., Entekhabi, D., 2023. Interaction between dry and hot extremes at a global scale using a cascade modeling framework. Nat. Commun. 14, 277. https://doi.org/10.1038/s41467-022-35748-7
Nicolai-Shaw, N., Zscheischler, J., Hirschi, M., Gudmundsson, L., Seneviratne, S.I., 2017. A drought event composite analysis using satellite remote-sensing based soil moisture. Remote Sens. Environ. 203, 216–225. https://doi.org/10.1016/j.rse.2017.06.014
OCO-2-Science-Team, Gunson, M., Eldering, A., 2020a. OCO-2 Level 2 bias-corrected XCO2 and other select fields from the full-physics retrieval aggregated as daily files, Retrospective processing V10r, Greenbelt, MD, USA, Goddard Earth Sciences Data and Information Services Center (GES DISC), Accessed: [2021.
OCO-2-Science-Team, Gunson, M., Eldering, A., 2020b. OCO-2 Level 2 bias-corrected solar-induced fluorescence and other select fields from the IMAP-DOAS algorithm aggregated as daily files, Retrospective processing V10r, Greenbelt, MD, USA, Goddard Earth Sciences Data and Information Services Center (GES DIS.
Pandey, S., Houweling, S., Lorente, A., Borsdorff, T., Tsivlidou, M., Anthony Bloom, A., Poulter, B., Zhang, Z., Aben, I., 2021. Using satellite data to identify the methane emission controls of South Sudan's wetlands. Biogeosciences 18, 557–572. https://doi.org/10.5194/bg-18-557-2021
Patra, P.K., Crisp, D., Kaiser, J.W., Wunch, D., Saeki, T., Ichii, K., Sekiya, T., Wennberg, P.O., Feist, D.G., Pollard, D.F., Griffith, D.W.T., Velazco, V.A., De Maziere, M., Sha, M.K.,

Roehl, C., Chatterjee, A., Ishijima, K., 2017. The Orbiting Carbon Observatory (OCO-2) tracks 2-3 peta-gram increase in carbon release to the atmosphere during the 2014-2016 El Niño. Sci. Rep. 7, 1–12. https://doi.org/10.1038/s41598-017-13459-0

Peters, W., Jacobson, A.R., Sweeney, C., Andrews, A.E., Conway, T.J., Masarie, K., Miller, J.B., Bruhwiler, L.M.P., Pétron, G., Hirsch, A.I., Worthy, D.E.J., Van Der Werf, G.R., Randerson, J.T., Wennberg, P.O., Krol, M.C., Tans, P.P., 2007. An atmospheric perspective on North American carbon dioxide exchange: CarbonTracker. Proc. Natl. Acad. Sci. U. S. A. 104, 18925–18930. https://doi.org/10.1073/pnas.0708986104

Philip, S.Y., Kew, S.F., Oldenborgh, G.J. Van, Yang, W., Vecchi, G.A., Anslow, F.S., Li, S., Seneviratne, S.I., Luu, L.N., Arrighi, J., Singh, R., Aalst, V., Hauser, M., Schumacher, D.L., Marghidan, C.P., Ebi, K.L., Vautard, R., Tradowsky, J., Coumou, D., Lehner, F., Rodell, C., Stull, R., Howard, R., Gillett, N., Otto, F.E.L., 2021. Rapid attribution analysis of the extraordinary heatwave on the Pacific Coast of the US and Canada June 2021 . World Weather Attrib. 119–123.

Poulter, B., Frank, D., Ciais, P., Myneni, R.B., Andela, N., Bi, J., Broquet, G., Canadell, J.G., Chevallier, F., Liu, Y.Y., Running, S.W., Sitch, S., Werf, G.R. Van Der, 2014. Contribution of semi-arid ecosystems to interannual variability of the global carbon cycle. Nature 509, 600–603. https://doi.org/10.1038/nature13376

Powell, T.L., Galbraith, D.R., Christoffersen, B.O., Harper, A., Imbuzeiro, H.M.A., Rowland, L., Almeida, S., Brando, P.M., da Costa, A.C.L., Costa, M.H., Levine, N.M., Malhi, Y., Saleska, S.R., Sotta, E., Williams, M., Meir, P., Moorcroft, P.R., 2013. Confronting model predictions of carbon fluxes with measurements of Amazon forests subjected to experimental drought. New Phytol. 200, 350–365. https://doi.org/10.1111/nph.12390

Rao, K., Anderegg, W.R.L., Sala, A., Martínez-Vilalta, J., Konings, A.G., 2019. Satellite-based vegetation optical depth as an indicator of drought-driven tree mortality. Remote Sens. Environ. 227, 125–136. https://doi.org/10.1016/j.rse.2019.03.026

Reichstein, M., Bahn, M., Ciais, P., Frank, D., Mahecha, M.D., Seneviratne, S.I., Zscheischler, J., Beer, C., Buchmann, N., Frank, D.C., Papale, D., Rammig, A., Smith, P., Thonicke, K., Van Der Velde, M., Vicca, S., Walz, A., Wattenbach, M., 2013. Climate extremes and the carbon cycle. Nature 500, 287–295. https://doi.org/10.1038/nature12350

Rodell, M., Famiglietti, J.S., 2001. An analysis of terrestrial water storage variations in Illinois with implications for the Gravity Recovery and Climate Experiment (GRACE). Water Resour. Res. 37, 1327–1339. https://doi.org/10.1029/2000WR900306

Schimel, D., Pavlick, R., Fisher, J.B., Asner, G.P., Saatchi, S., Townsend, P., Miller, C., Frankenberg, C., Hibbard, K., Cox, P., 2015. Observing terrestrial ecosystems and the carbon cycle from space. Glob. Chang. Biol. 21, 1762–1776. https://doi.org/10.1111/gcb.12822

Schuh, A.E., Byrne, B., Jacobson, A.R., Crowell, S.M.R., Deng, F., Baker, D.F., Johnson, M.S., Philip, S., Weir, B., 2022. On the role of atmospheric model transport uncertainty in estimating the Chinese land carbon sink. Nature 603, E13–E14. https://doi.org/10.1038/s41586-021-04258-9

Schwalm, C.R., Anderegg, W.R.L., Michalak, A.M., Fisher, J.B., Biondi, F., Koch, G., Litvak, M., Ogle, K., Shaw, J.D., Wolf, A., Huntzinger, D.N., Schaefer, K., Cook, R., Wei, Y., Fang, Y., Hayes, D., Huang, M., Jain, A., Tian, H., 2017. Global patterns of drought recovery. Nature 548, 202–205. https://doi.org/10.1038/nature23021

Sellers, P.J., Schimel, D.S., Moore, B., Liu, J., Eldering, A., 2018. Observing carbon cycle–

climate feedbacks from space. Proc. Natl. Acad. Sci. U. S. A. 115, 7860–7868. https://doi.org/10.1073/pnas.1716613115
Sheffield, J., Wood, E.F., 2008. Projected changes in drought occurrence under future global warming from multi-model, multi-scenario, IPCC AR4 simulations. Clim. Dyn. 31, 79–105. https://doi.org/10.1007/s00382-007-0340-z
Short Gianotti, D.J., Rigden, A.J., Salvucci, G.D., Entekhabi, D., 2019. Satellite and Station Observations Demonstrate Water Availability's Effect on Continental-Scale Evaporative and Photosynthetic Land Surface Dynamics. Water Resour. Res. https://doi.org/10.1029/2018WR023726
Sitch, S., Smith, B., Prentice, I.C., Arneth, A., Bondeau, A., Cramer, W., Kaplan, J.O., Levis, S., Lucht, W., Sykes, M.T., Thonicke, K., Venevsky, S., 2003. Evaluation of ecosystem dynamics, plant geography and terrestrial carbon cycling in the LPJ dynamic global vegetation model. Glob. Chang. Biol. 9, 161–185. https://doi.org/10.1046/j.1365-2486.2003.00569.x
Slette, I.J., Post, A.K., Awad, M., Even, T., Punzalan, A., Williams, S., Smith, M.D., Knapp, A.K., 2019. How ecologists define drought, and why we should do better. Glob. Chang. Biol. 25, 3193–3200. https://doi.org/10.1111/gcb.14747
Slette, I.J., Smith, M.D., Knapp, A.K., Vicente-Serrano, S.M., Camarero, J.J., Beguería, S., 2020. Standardized metrics are key for assessing drought severity. Glob. Chang. Biol. 26, e1–e3. https://doi.org/10.1111/gcb.14899
Smith, M.D., 2011. An ecological perspective on extreme climatic events: A synthetic definition and framework to guide future research. J. Ecol. 99, 656–663. https://doi.org/10.1111/j.1365-2745.2011.01798.x
Smith, W.K., Biederman, J.A., Scott, R.L., Moore, D.J.P., He, M., Kimball, J.S., Yan, D., Hudson, A., Barnes, M.L., MacBean, N., Fox, A.M., Litvak, M.E., 2018. Chlorophyll Fluorescence Better Captures Seasonal and Interannual Gross Primary Productivity Dynamics Across Dryland Ecosystems of Southwestern North America. Geophys. Res. Lett. 45, 748–757. https://doi.org/10.1002/2017GL075922
Stocker, B.D., Tumber-dávila, S.J., Konings, A.G., Anderson, M.C., Hain, C., Jackson, R.B., 2023. Global patterns of water storage in the rooting zones of vegetation. Nat. Geosci. https://doi.org/https://doi.org/10.1038/s41561-023-01125-2
Teixeira, J., 2013. AIRS/Aqua L3 Daily Standard Physical Retrieval (AIRS-only) 1 degree x 1 degree V006, Greenbelt, MD, USA, Goddard Earth Sciences Data and Information Services Center (GES DISC), Accessed: 04.25.20, doi:10.5067/Aqua/A.
Tuttle, S.E., Salvucci, G.D., 2017. Confounding factors in determining causal soil moisture-precipitation feedback. Water Resour. Res. 5531–5544. https://doi.org/10.1002/2016WR019869
Varon, D.J., Jacob, D.J., McKeever, J., Jervis, D., Durak, B.O.A., Xia, Y., Huang, Y., 2018. Quantifying methane point sources from fine-scale satellite observations of atmospheric methane plumes. Atmos. Meas. Tech. 11, 5673–5686. https://doi.org/10.5194/amt-11-5673-2018
Vicca, S., Balzarolo, M., Filella, I., Granier, A., Herbst, M., Knohl, A., Longdoz, B., Mund, M., Nagy, Z., Pintér, K., Rambal, S., Verbesselt, J., Verger, A., Zeileis, A., Zhang, C., Peñuelas, J., 2016. Remotely-sensed detection of effects of extreme droughts on gross primary production. Sci. Rep. 6, 1–13. https://doi.org/10.1038/srep28269
Wang, W., Ciais, P., Nemani, R.R., Canadell, J.G., Piao, S., Sitch, S., White, M.A., Hashimoto,

H., Milesi, C., Myneni, R.B., 2013. Variations in atmospheric CO2 growth rates coupled with tropical temperature. Proc. Natl. Acad. Sci. U. S. A. 110, 13061–13066. https://doi.org/10.1073/pnas.1314920110

Weir, B., Crisp, D., O'Dell, C.W., Basu, S., Chatterjee, A., Kolassa, J., Oda, T., Pawson, S., Poulter, B., Zhang, Z., Ciais, P., Davis, S.J., Liu, Z., Ott, L.E., 2021. Regional impacts of COVID-19 on carbon dioxide detected worldwide from space. Sci. Adv. 7, 1–10. https://doi.org/10.1126/sciadv.abf9415

Werner, C., Meredith, L.K., Ladd, S.N., Ingrisch, J., Kübert, A., van Haren, J., Bahn, M., Bailey, K., Bamberger, I., Beyer, M., Blomdahl, D., Byron, J., Daber, E., Deleeuw, J., Dippold, M.A., Fudyma, J., Gil-Loaiza, J., Honeker, L.K., Hu, J., Huang, J., Klüpfel, T., Krechmer, J., Kreuzwieser, J., Kühnhammer, K., Lehmann, M.M., Meeran, K., Misztal, P.K., Ng, W.R., Pfannerstill, E., Pugliese, G., Purser, G., Roscioli, J., Shi, L., Tfaily, M., Williams, J., 2021. Ecosystem fluxes during drought and recovery in an experimental forest. Science (80-.). 374, 1514–1518. https://doi.org/10.1126/science.abj6789

Wiese, D.N., Yuan, D.-N., Boening, C., Landerer, F.W., Watkins, M.M., 2019. JPL GRACE Mascon Ocean, Ice, and Hydrology Equivalent Water Height RL06 CRI Filtered Version 02. Ver. 02. PO.DAAC, CA, USA. Dataset accessed [2021-11-04] at https://doi.org/10.5067/TEMSC-3JC62.

Williams, A.P., Cook, B.I., Smerdon, J.E., 2022. Rapid intensification of the emerging southwestern North American megadrought in 2021. Nat. Clim. Chang. 12, 232–234.

Wolf, S., Keenan, T.F., Fisher, J.B., Baldocchi, D.D., Desai, A.R., Richardson, A.D., Scott, R.L., Law, B.E., Litvak, M.E., Brunsell, N.A., Peters, W., Van Der Laan-Luijkx, I.T., 2016. Warm spring reduced carbon cycle impact of the 2012 US summer drought. Proc. Natl. Acad. Sci. U. S. A. 113, 5880–5885. https://doi.org/10.1073/pnas.1519620113

Yang, H., Munson, S.M., Huntingford, C., Carvalhais, N., Knapp, A.K., Li, X., Peñuelas, J., Zscheischler, J., Chen, A., 2023. The detection and attribution of extreme reductions in vegetation growth across the global land surface. Glob. Chang. Biol. 2351–2362. https://doi.org/10.1111/gcb.16595

Zhang, Z., Zimmermann, N.E., Calle, L., Hurtt, G., Chatterjee, A., Poulter, B., 2018. Enhanced response of global wetland methane emissions to the 2015-2016 El Niño-Southern Oscillation event. Environ. Res. Lett. 13. https://doi.org/10.1088/1748-9326/aac939

Zhou, S., Park Williams, A., Berg, A.M., Cook, B.I., Zhang, Y., Hagemann, S., Lorenz, R., Seneviratne, S.I., Gentine, P., 2019. Land–atmosphere feedbacks exacerbate concurrent soil drought and atmospheric aridity. Proc. Natl. Acad. Sci. U. S. A. 116, 18848–18853. https://doi.org/10.1073/pnas.1904955116

Zscheischler, J., Mahecha, M.D., Harmeling, S., Reichstein, M., 2013. Detection and attribution of large spatiotemporal extreme events in Earth observation data. Ecol. Inform. 15, 66–73. https://doi.org/10.1016/j.ecoinf.2013.03.004

Zscheischler, Jakob, Mahecha, M.D., Von Buttlar, J., Harmeling, S., Jung, M., Rammig, A., Randerson, J.T., Schölkopf, B., Seneviratne, S.I., Tomelleri, E., Zaehle, S., Reichstein, M., 2014. A few extreme events dominate global interannual variability in gross primary production. Environ. Res. Lett. 9. https://doi.org/10.1088/1748-9326/9/3/035001

Zscheischler, J., Reichstein, M., Harmeling, S., Rammig, A., Tomelleri, E., Mahecha, M.D., 2014. Extreme events in gross primary production: A characterization across continents. Biogeosciences 11, 2909–2924. https://doi.org/10.5194/bg-11-2909-2014

1119